Limitations of grain refinement in solute-modified CoCrNi: The role of constitutional supercooling in PBF-LB

Additive Manufacturing 127 (2026) 105279

Contents lists available at ScienceDirect

Additive Manufacturing

journal homepage: www.elsevier.com/locate/addma

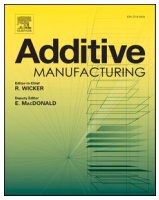

Limitations of grain refinement in solute-modified CoCrNi: The role of constitutional supercooling in PBF-LB

Ameer Hamza Khan [a], Sri Bala Aditya Malladi [b], Marcio Sangali Cristino da Silva [a,c], João Felipe Queiroz Rodrigues [a], Sheng Guo [b], Kaio Niitsu Campo [a,*]

[a] School of Mechanical Engineering, University of Campinas, Campinas, Brazil
[b] Department of Industrial and Materials Science, Chalmers University of Technology, Göteborg, Sweden
[c] Federal Institute of Education, Science and Technology of São Paulo, São João da Boa Vista, Brazil

ARTICLE INFO

Keywords:
Additive manufacturing
Powder bed fusion - laser beam
Medium-entropy alloy
CoCrNi
Constitutional supercooling
Grain refinement

ABSTRACT

Additive manufacturing of medium-entropy alloys offers unique opportunities for fabricating complex metallic components with enhanced mechanical properties. However, this processing route is often challenged by the formation of columnar grains and microstructural anisotropy. In this study, a solute-based strategy leveraging constitutional supercooling was explored to promote grain refinement in a CoCrNi alloy. Ti was selected through thermodynamic calculations due to its high growth restriction factor (Q) and favorable solubility, and a $(CoCrNi)_{97}Ti_3$ (at%) composition was produced via in-situ alloying using powder bed fusion - laser beam. Although grain size refinement was not observed, Ti addition disrupted columnar grain growth and promoted a more equiaxed morphology, likely due to modified melt pool dynamics associated with in-situ alloying. Complementary casting and single-track experiments confirmed that steep thermal gradients inherent to PBF-LB processing can suppress solute-driven grain refinement. Thermal analysis further revealed lower experimental Q values compared to predictions, evidencing limitations in the thermodynamic data employed. Additionally, the high solidification rates during laser processing slightly reduced segregation, contributing to a slightly lower effective Q value. These findings highlight the importance of linking solute selection with process-specific solidification conditions and provide new insights into the combined effects of alloy chemistry, melt pool dynamics, and thermal gradients in medium-entropy alloys processed by additive manufacturing.

1. Introduction

Recent advances in metallic materials research have been strongly influenced by two key areas: additive manufacturing (AM) and compositionally complex alloys, particularly high-entropy alloys (HEAs) and medium-entropy alloys (MEAs). Although AM primarily relates to fabrication and processing techniques, and HEA/MEAs to materials design and selection, both share the fundamental characteristic of significantly broadening the horizons of the field. AM enables a substantial expansion in the capacity to produce geometric shapes, while the concept of HEAs and MEAs extends compositional possibilities, leading to a wide range of microstructures and properties. In this context, these combined approaches can enable new engineering processes and products, promoting technological innovation and sustainable progress. As such, they constitute a highly dynamic and stimulating field of research.

MEAs often exhibit properties that surpass those of HEAs. A notable example within the MEA class is the CoCrNi alloy, which demonstrates superior mechanical behavior compared to its parent alloy, CoCrFeMnNi [1]. The CoCrNi alloy features a face-centered cubic (FCC) structure with a balanced combination of reasonable strength and high ductility at both ambient and cryogenic temperatures. Additionally, it showcases exceptional fracture toughness and outstanding resistance to corrosion and oxidation at elevated temperatures [2–5]. Given this favorable combination of properties, there has been growing interest in exploring the CoCrNi MEA through AM [6–10].

One of the primary challenges in AM is the formation of coarse, columnar grain structures, which can lead to anisotropy and heterogeneity in both the microstructure and mechanical properties. Anisotropy and columnar grains can be beneficial in certain applications and may even be intentionally induced, particularly when the loading direction is well defined or when enhanced creep resistance is desired. However,

* Corresponding author.
E-mail address: kaionc@unicamp.br (K.N. Campo).

https://doi.org/10.1016/j.addma.2026.105279
Received 29 January 2026; Received in revised form 21 May 2026; Accepted 23 June 2026
Available online 28 June 2026

they are generally considered undesirable for broader structural applications. In such cases, achieving a more isotropic material is preferred, as it facilitates more reliable prediction of mechanical behavior under various loading conditions, simplifies simulation modeling, and helps avoid unwanted variations in mechanical properties across different geometries or build orientations. Consequently, many studies have focused on strategies to eliminate or minimize anisotropy in AM-produced components [11–17]. In the case of CoCrNi, Li et al. [10] showed that a high degree of mechanical anisotropy and microstructural heterogeneity can arise depending on the processing parameters used in the powder bed fusion - laser beam (PBF-LB) process.

Another major concern in AM is cracking. In the CoCrNi alloy processed via PBF-LB, solidification cracking has been reported, mainly influenced by the selected processing parameters. Niu et al. [7] found that residual stresses increase with higher volumetric energy densities (VEDs), leading to the formation of cracks in samples processed with high energy inputs. These solidification cracks form when the thin liquid film at the end of solidification is unable to withstand the tensile stresses generated during processing. Residual stress is a well-known issue in AM, arising from the highly localized and cyclic nature of thermal input.

To mitigate solidification cracking, several strategies have been proposed, including the optimization of processing parameters, grain refinement, and segregation engineering [18]. Among these, grain refinement has proven particularly effective, as fine equiaxed grains are significantly less susceptible to cracking, while also contributing to enhanced and more isotropic mechanical properties. For example, Li et al. [19] showed that in Al–Cu–Mg–Mn–Zr alloys the formation of fully equiaxed grains through a columnar-to-equiaxed transition (CET) resulted in crack-free samples. This is because liquid feeding at the end of solidification becomes easier in fine equiaxed grains, thereby decreasing cracking susceptibility. Therefore, promoting grain refinement by inducing a CET, together with careful control of processing parameters to reduce thermal stresses, has emerged as a reliable strategy to suppress solidification cracking in PBF-LB-processed materials [19–21].

Working to prevent large columnar grains and periodic cracks, Martin et al. [22] demonstrated in a seminal study that nanoparticle additions could promote equiaxed grain formation in high-strength Al alloys processed by PBF-LB through heterogeneous nucleation-assisted grain refinement, enabling the AM of alloys previously considered incompatible with the process. Following this work, several studies explored inoculation-based approaches to promote CET under AM conditions [22–24]. Another widely explored strategy for promoting CET involves the use of solutes to enhance constitutional supercooling. A notable example is provided by Zhang et al. [11], who compared Ti−6Al-4V and Ti-Cu alloys with markedly different capacities for constitutional supercooling. Ti−6Al-4V, which exhibits relatively limited constitutional supercooling, developed large columnar grains, whereas the Ti−8.5Cu alloy produced fine equiaxed grains. Subsequent investigations revealed that classical grain refinement theories based solely on constitutional supercooling are insufficient to fully explain grain formation during AM. Under the extremely high thermal gradients and solidification velocities characteristic of this processing route, grain nucleation is also strongly influenced by thermal undercooling generated by the lag between dendrite growth velocity and the moving thermal field [25,26]. Nonetheless, Tan et al. [26] showed that, despite the extremely high cooling rates in PBF-LB, solute additions are still required to generate sufficient undercooling for heterogeneous nucleation within the melt pool. In an interesting recent work, Fan et al. [27] demonstrated that the concept of promoting grain refinement through enhanced constitutional supercooling is not restricted to metallic systems. Solute additions to yttria-stabilized zirconia during laser AM promoted a transition from coarse columnar grains to fine equiaxed grains, significantly suppressing cracking in the fabricated ceramic components.

Given the promising technological relevance of the CoCrNi-based MEAs for AM applications, understanding and controlling their solidification behavior during PBF-LB processing is of considerable importance. However, CoCrNi still exhibits a strong tendency for epitaxial columnar grain growth due to the steep thermal gradients developed in the process [6–10]. Since no effective nucleant has yet been reported for CoCrNi and its derivative compositions, grain refinement during AM primarily relies on generating sufficient undercooling, which is influenced by both alloy composition and processing parameters. Therefore, this investigation aims to select a suitable solute for modifying the CoCrNi alloy and to evaluate the effectiveness of constitutional supercooling in promoting grain refinement during PBF-LB, with particular emphasis on the relationships between processing conditions, solidification behavior, and grain morphology.

2. Solute selection

Grain size and morphology are influenced by the dynamic interplay between nucleation and growth processes, which, while occurring independently, are strongly interconnected. This relationship can be effectively described by the Interdependence Theory, which provides a framework for linking grain formation to nucleant selection [28]. This theory offers valuable insights into the mechanisms of grain refinement and enables more accurate predictions of grain size. According to this theory, the grain size (d_{gs}) results from three main contributions: (i) the distance the grain must grow until it generates sufficient constitutional supercooling (ΔT_{CS}) to allow nucleation on a particle characterized by a given $\Delta T_{n\text{-}min}$ (the minimum undercooling required for nucleation), (ii) the diffusion length, defined as the distance from the solid-liquid interface to the point where ΔT_{CS} equals $\Delta T_{n\text{-}min}$, and (iii) the average distance between active nucleant particles. The combined effect of the first two contributions defines what is termed the nucleation-free zone [28].

A larger nucleation-free zone results in a larger final grain size. This zone can be reduced by increasing the constitutional supercooling, which is strongly influenced by solute elements. Accordingly, the effect of solute concentration on grain size during solidification can be described by the following equation [28,29]:

$$d_{gs} = \quad a + \frac{b}{Q} \tag{1}$$

where a and b are constants, and Q is the growth restriction factor, given by [29]:

$$Q = m_l C_0 (k - 1) \tag{2}$$

where m_l is the slope of the liquidus line, C_0 is the solute concentration, and k is the partition coefficient.

Eq. 2 applies to binary systems. For multicomponent alloys, however, the restriction factor is given by [29]:

$$Q = \left(\frac{\partial (\Delta T_{CS})}{\partial f_s} \right)_{f_s \to 0} \tag{3}$$

where f_s is the solid fraction.

The growth restriction factor measures how quickly constitutional supercooling develops in front of the solid-liquid (S/L) interface. For the CoCrNi alloy, the efficiency of typical solutes, expressed by the Q parameter, was evaluated through thermodynamic calculations using the Thermo-Calc® software with the TCHEA6 database [30]. The Q parameter was obtained by applying Eq. 3 to Scheil solidification curves generated for different alloy compositions. A schematic representation of the Q parameter determination procedure is shown in Fig. 1a. In this method [29,31], the Scheil solidification is simulated in the software, and $\Delta T_{CS} = T_l - T$, where T_l is the liquidus temperature and T is the actual temperature, is calculated as a function of f_s. The Q value corresponds to the initial slope of this ΔT_{CS}—f_s curve. The corresponding results are shown in Fig. 1b. The maximum solute concentration was

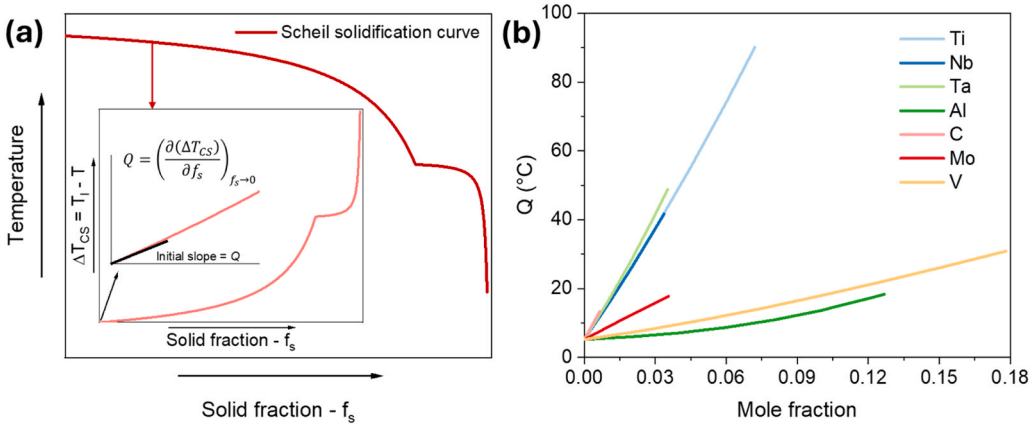

Fig. 1. (a) Schematic representation of the procedure used to determine the growth restriction factor (*Q*) from Scheil solidification simulations, and (b) calculated *Q* values for various solutes in the CoCrNi alloy, obtained through thermodynamic calculations using the Thermo-Calc® software with the TCHEA6 database.

limited by the maximum solubility of the solute in the FCC phase. As observed, Ti stands out as the most promising solute, exhibiting a significant effect on *Q* along with relatively high solubility in the FCC phase. This allows for the attainment of high *Q* values with Ti, explaining its selection for the development of this investigation.

Other investigations have identified Ti as a promising alloying addition to CoCrNi. In a recent study, Chang and Hsueh [32] investigated the effects of Ti additions on the microstructure and mechanical properties of $(CoCrNi)_{100-x}Ti_x$ alloys, with x ranging from 0 to 4 (at%). The samples were produced through arc melting, followed by hot rolling and annealing at 900 °C for 1 h. Their findings revealed that a single-phase FCC solid solution microstructure was retained up to the $(CoCrNi)_{98}Ti_2$ composition after annealing. At higher Ti concentrations, $(Ni,Co)_3Ti$ precipitates were observed. The incorporation of Ti into the solid solution also caused lattice distortion due to its larger atomic radius compared to other constituent elements. In addition, increasing Ti content promoted grain refinement, which, together with precipitation and solid-solution strengthening, contributed to the observed improvement in mechanical strength [32]. However, the benefits of this strengthening effect appear to have a limit: in another investigation, at a Ti concentration as high as 6 at%, the alloy exhibited an ultimate tensile strength of nearly 2 GPa, but this was accompanied by a severe loss of ductility, which dropped to below 3% [33].

Based on these studies [32,33], the $(CoCrNi)_{97}Ti_3$ alloy was found to offer an excellent balance between tensile strength and ductility. Specifically, it exhibited a yield strength of approximately 1080 MPa, an ultimate tensile strength of about 1430 MPa, and an elongation to fracture of nearly 40% [32]. This combination of properties underscores its potential for a wide range of engineering applications. Therefore, a Ti concentration of 3 at% was selected in the present study to modify the CoCrNi alloy.

3. Experimental

Spherical gas-atomized Ti-Cp grade 2 (15–45 μm, AP&C, Colibrium Additive) and CoCrNi (15–45 μm, Höganäs AB) powders were mixed at the desired atomic ratio for at least 3 h under an Ar atmosphere prior to printing via PBF-LB. Details of the powder characterization are provided in Fig. S1 of the Supplementary Information (SI). The printing was performed on an OmniSint−160 machine (OmniTek Tecnologia, Brazil), equipped with a Yb:YAG fiber laser with a wavelength of 1070 nm, a spot size of 80 μm, and a maximum power of 500 W [34]. Initially, processing parameters were evaluated by printing cylindrical samples with both diameter and height of 5 mm. The variables studied included laser power ($P = 100$, 150, and 200 W) and laser scan speed ($v = 500$, 700, and 900 mm/s), while the layer thickness ($t = 30$ μm) and hatch space ($h = 80$ μm) were kept constant. A standard 67° rotation was applied between layers, and scanning followed a zig-zag pattern. The composition and densification results from these experiments are presented in Fig. S2 of the SI.

Specific parameters were selected and subsequently used to produce larger samples of both the original CoCrNi and the Ti-modified $(CoCrNi)_{97}Ti_3$ alloys. The printing process began with one composition and transitioned to the other, taking advantage of the machine's dual-hopper system, which enables independent powder feeding and facilitates straightforward compositional changes during processing [34]. Cylindrical samples (10 mm in diameter, 20 mm in height) were produced, consisting of half CoCrNi and half $(CoCrNi)_{97}Ti_3$, with the building direction (BD) aligned along the height. For comparison, CoCrNi and Ti-modified CoCrNi alloys were also fabricated by casting, using high-purity metals (>99.9%). The samples were arc-melted multiple times in a high-purity Ar atmosphere with a Ti getter, using an Edmund Bühler GmbH arc melter and a water-cooled copper hearth. The molten alloys were then drop cast into a Cu mold with dimensions of $10 \times 10 \times 40$ mm^3.

Microstructural characterization was conducted using scanning electron microscopy (SEM) on FEI Quanta 650 FEG and LEO Gemini 1550 microscopes, both equipped with energy-dispersive X-ray spectroscopy (EDS) and electron backscatter diffraction (EBSD) systems. EBSD data were processed using AZtecCrystal software (Oxford Instruments). Transmission electron microscopy (TEM) characterization was performed using a JEOL JEM-2100F microscope. The TEM lamella was prepared using focused ion beam (FIB) milling on an FEI Helios NanoLab 660 dual-beam system, employing the lift-out technique. Visible-light microscopy (VLM) was performed using an Olympus BX60 microscope. Differential scanning calorimetry (DSC) measurements were performed using a Netzsch STA 449 thermal analyzer, with a scan rate of 10 °C/min in a dynamic Ar atmosphere. As previously mentioned, CALPHAD calculations were conducted using the Thermo-Calc® software with the TCHEA6 database.

4. Results

4.1. Compositional homogeneity and phase formation

Achieving a homogeneous composition during in-situ alloying by PBF-LB can be challenging [35]. In the present study, several factors may contribute to alloy homogenization. First, the melting points of Ti (1670 °C [36]) and CoCrNi (1435 °C [37]) are relatively close, facilitating concurrent melting. Additionally, Ti exhibits a strong negative enthalpy of mixing with the elements in the CoCrNi alloy, particularly with Co and Ni, which promotes exothermic reactions during

processing, associated with bond formation or intermetallic tendencies [35,38,39]. However, although the initial powder mixing resulted in a reasonably homogeneous distribution of Ti particles (Fig. S1 of the SI), the reduced melt pool size characteristic of PBF-LB, combined with the powder size, implies that each melt pool incorporates only a limited number of particles [40]. As a result, local variations in composition are expected from melt pool to melt pool [40]. Furthermore, under the present processing conditions, the rapid solidification velocities limit Marangoni convection and atomic diffusion, preventing the complete removal of compositional gradients in the liquid. Although higher energy inputs could be explored to enhance liquid homogenization, such conditions would also promote microstructural coarsening and increase the susceptibility to microcracking [7].

Fig. 2a shows SEM-EDS maps illustrating the Ti distribution across samples processed with varying VED values, calculated using the equation: $VED = P/vht$ [41]. Although VED is a simplified process parameter and does not uniquely describe the melt pool thermal conditions during PBF-LB, it provides a practical basis for comparing relative processing trends. As expected, low energy inputs resulted in a higher prevalence of unmelted Ti particles, with one example (C3) highlighted in Fig. 2b. Fig. 2c shows detailed Ti distribution maps for two selected conditions (C1 and C7, indicated in the insets of Fig. 2a). C7, corresponding to the highest VED employed, clearly exhibits a more uniform Ti distribution compared to C1, which was processed with an intermediate VED. Similar to observations in the in-situ alloying of Ti into equiatomic CoCrFeNi, Ti tended to segregate along the melt pool boundaries due to its higher melting point, leading it to solidify first [42].

The addition of Ti did not alter the FCC structure of CoCrNi, regardless of VED, as confirmed by X-ray diffraction patterns shown in Fig. S3 of the SI. This is consistent with the high cooling rates inherent to the PBF-LB process, which favor full retention of the FCC phase. A more detailed analysis of the phases formed was conducted using TEM, and the results are presented in Fig. 3 for a typical as-printed (AP) sample. Due to the compositional heterogeneity, two distinct regions were analyzed: one Ti-poor and the other Ti-rich. The results shown in Figs. 3a to 3c correspond to the Ti-poor region, where the analyzed area contained approximately 1 at% Ti. In Fig. 3a, a bright-field scanning transmission electron microscopy (BF-STEM) image shows the absence of the typical cellular substructures commonly observed in CoCrNi alloys processed by PBF-LB [43]. Furthermore, the selected area electron diffraction (SAED) pattern (Fig. 3b) confirms the FCC crystal structure of the material. STEM-EDS elemental mapping (Fig. 3c) indicates no significant solute segregation during solidification. However, the presence of rounded Ti-rich nanoparticles is evident, which were identified as Ti oxides based on the STEM-EDS line scan analysis shown in Fig. S4a of the SI.

Results for the Ti-rich region (Ti concentration of ~15 at%) are presented in Figs. 3d to 3f. In this region, cellular substructures were observed, as shown in the BF-STEM image in Fig. 3d. The microstructure remains predominantly composed of the FCC phase, as indicated by the SAED pattern in Fig. 3e. Notably, neither the metastable cubic $L1_2$-type [42] nor the stable hexagonal $D0_{24}$-type [32] Ni_3Ti phases were detected in this Ti-rich area. The STEM-EDS elemental mapping (Fig. 3f) reveals that Ti segregated to the cellular walls, where Cr was depleted, while Co and Ni concentrations remained relatively uniform. As shown in Figs. S4b and S4c of the SI, the formation of Cr-rich sigma (σ) phase was detected. However, because its distribution was limited to localized, highly Ti-enriched regions, the σ phase did not significantly affect the overall microstructure.

4.2. Grain size and morphology

The grain size, expressed in terms of equivalent diameter and determined from the EBSD results, is shown as a function of processing conditions in Fig. 4a. A clear trend is observed: grain size increased with increasing VED, as further evidenced by the equivalent diameter distributions presented in Fig. 4b. The mean grain size ranged from 10.7 to 18.2 μm. This behavior is expected, as VED influences the thermal history and the degree of undercooling in the melt pool. Lower VED values generally lead to increased cooling rates and reduced melt pool dimension, which can enhance the undercooling at the S/L interface and favor microstructural refinement [44].

Fig. 4a also revealed that the grains became increasingly elongated with higher VED. This observation is supported by the aspect ratio (AR) results shown in Fig. 5a, where the AR increased from 2.2 to 2.7 with increasing VED. Grains are typically considered equiaxed when their AR is below 2 [45,46]. Based on this criterion, the microstructure can be further classified by the volume fraction of equiaxed grains (φ). A microstructure is considered fully equiaxed when $\varphi > 0.49$, and fully columnar when $\varphi < 0.0066$, with intermediate values indicating a mixed grain structure [47]. In this context, Fig. 5b shows φ as a function of VED. Most processing conditions, including those with low and intermediate VED values, resulted in fully equiaxed microstructures. Under these conditions, approximately half of the area fraction (estimation of volume fraction) consisted of grains with an AR below 2, while

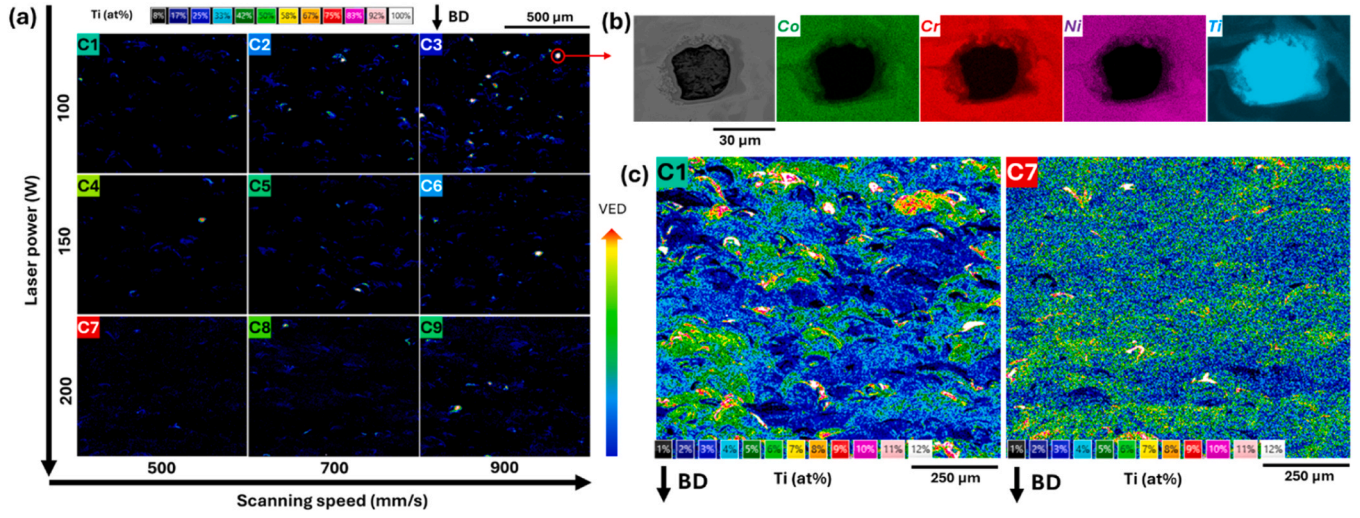

Fig. 2. EDS-SEM elemental mapping of the as-printed samples: (a) Ti distribution across samples fabricated with different VED values, (b) example of an unmelted Ti particle observed in a low VED condition (C3), and (c) detailed Ti distribution maps for selected processing conditions.

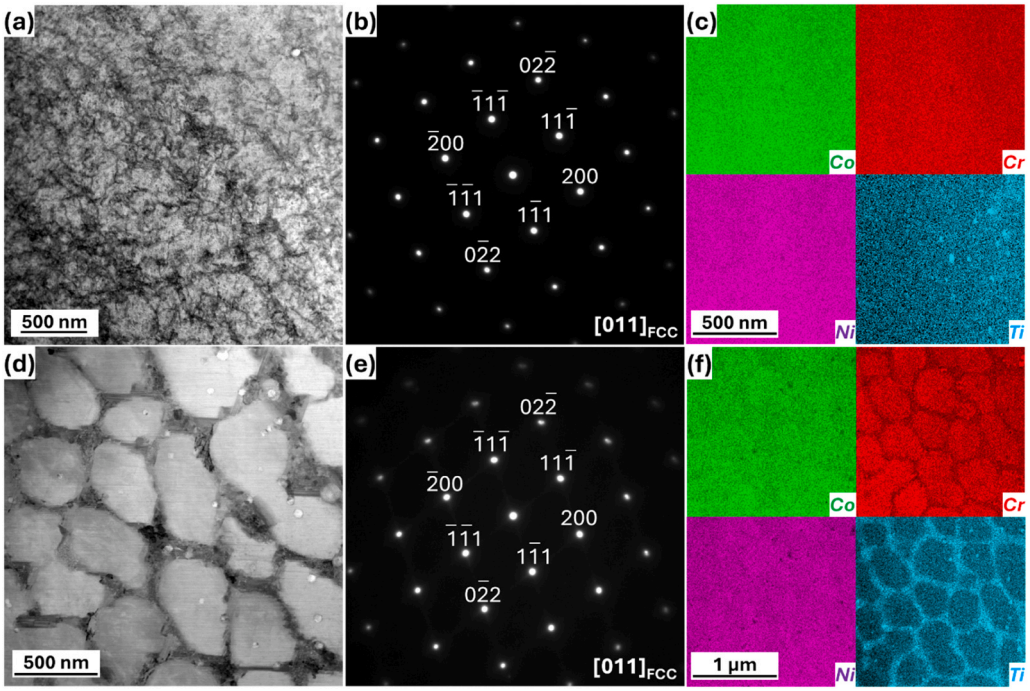

Fig. 3. TEM analysis of regions with different Ti concentrations in a typical as-printed sample. (a) BF-STEM image, (b) SAED pattern, (c) and STEM-EDS elemental mapping in the Ti-poor region (~1 at% Ti). (d) BF-STEM image, (e) SAED pattern, and (f) STEM-EDS elemental mapping in the Ti-rich region (~15 at% Ti).

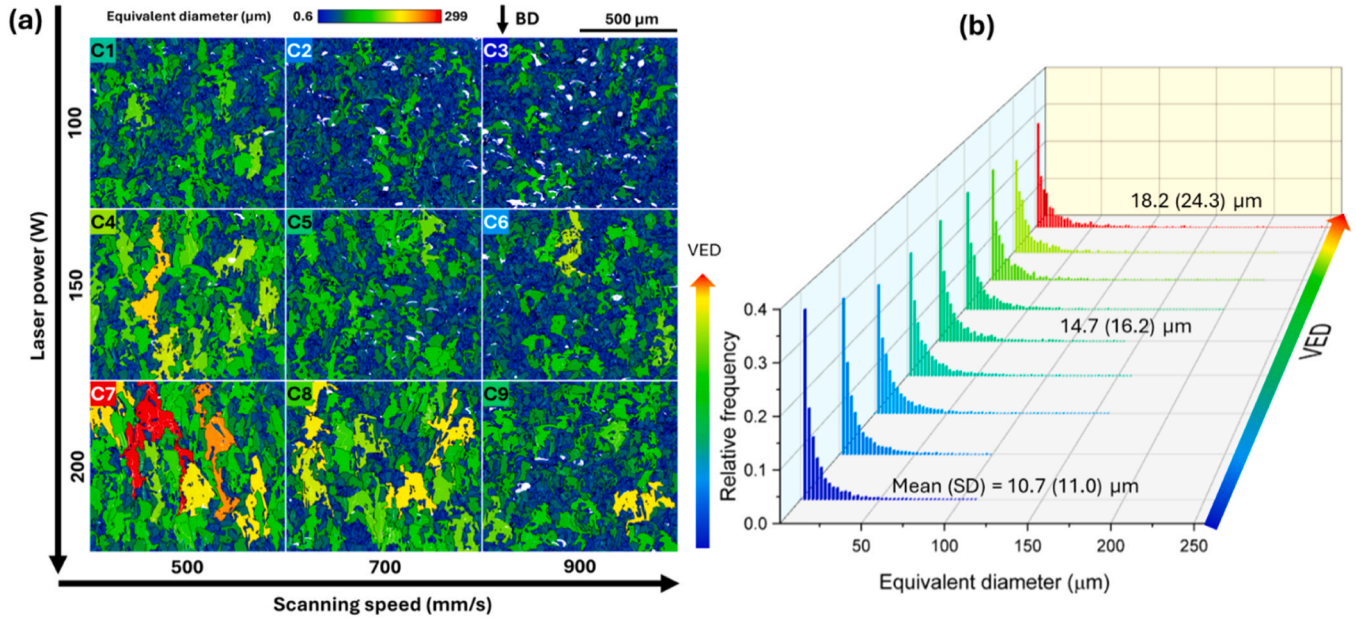

Fig. 4. EBSD analysis of grain size in the as-printed samples: (a) equivalent grain diameter maps for samples processed at different VED values (black lines indicate high-angle grain boundaries, ≥15°), and (b) equivalent diameter distribution as a function of VED.

80–90% of the area fraction corresponded to grains with an AR below 3 (Fig. 5b).

4.3. Texture

The effect of VED on the crystallographic texture was evaluated using EBSD, and the results are presented in Fig. 6. In Fig. 6a, inverse pole figure (IPF) maps along the Z direction are shown for the lowest, intermediate, and highest VED conditions (C3, C5, and C7, respectively), while the corresponding inverse pole figures are displayed in Fig. 6b. Based on the maximum multiple of uniform distribution (MUD) values, it is evident that the texture intensity increased with VED. The sample produced with the lowest heat input exhibited a nearly random or weak texture. In contrast, higher heat inputs resulted in stronger texture development. The texture in CoCrNi alloys produced by AM has been reported to vary between < 100 > //BD and < 110 > //BD orientations [10,48], which aligns with the trends observed in this study. This variation arises because FCC metals tend to grow along the < 100 > direction. Depending on the geometry of the melt pool, this growth direction may align more or less with the BD: shallow melt pools

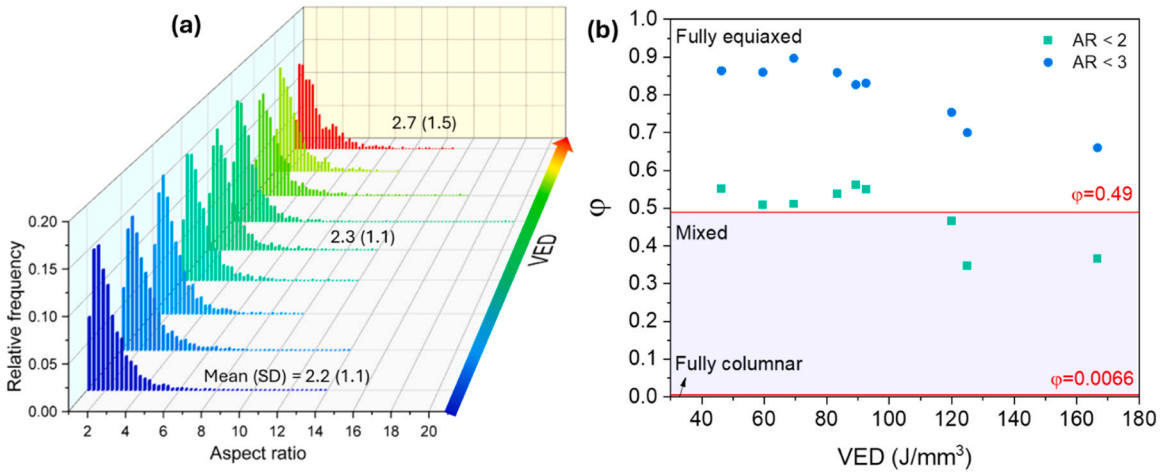

Fig. 5. (a) Distribution of the aspect ratio (AR) of the grains determined via EBSD as a function of VED, and (b) fraction of equiaxed grains (φ) as a function of VED.

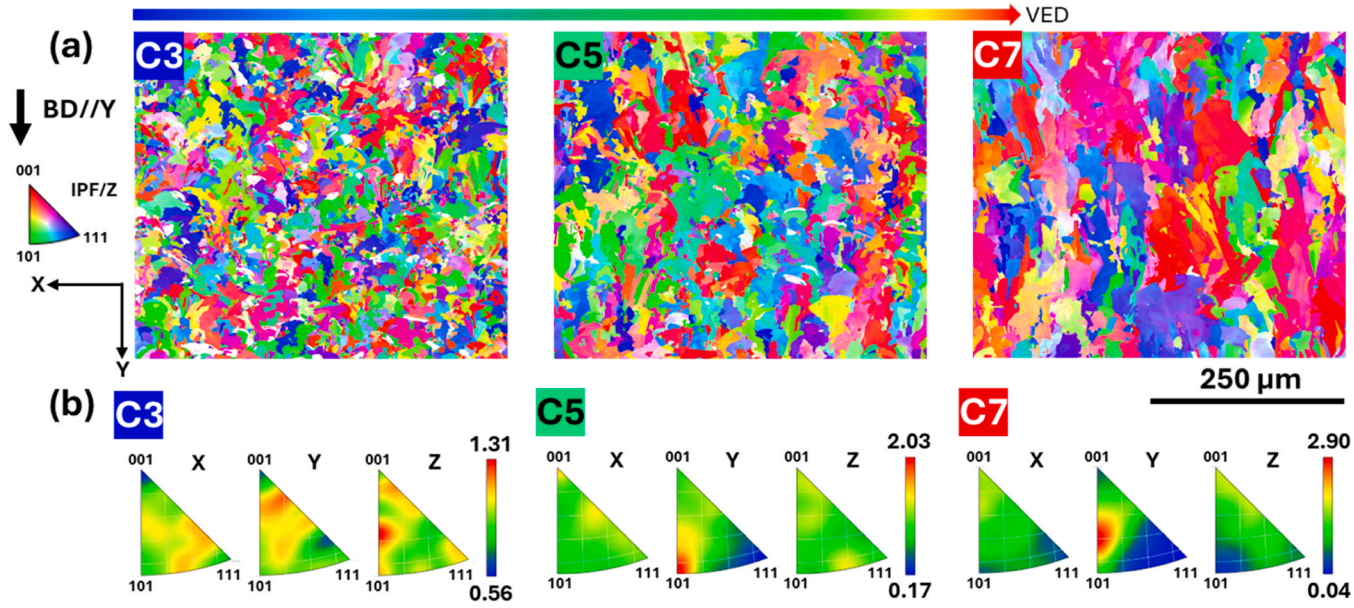

Fig. 6. EBSD analysis of crystallographic texture for the lowest, intermediate, and highest VED conditions (C3, C5, and C7, respectively): (a) IPF-Z maps and (b) corresponding inverse pole figures.

typically favor a < 100 > //BD texture, whereas deeper melt pools tend to promote a < 110 > //BD texture [10].

4.4. *Microstructural comparison between Ti-modified and base CoCrNi alloys*

Based on the previous results, two VED conditions were selected to compare the microstructure of $(CoCrNi)_{97}Ti_3$ with that of the original CoCrNi alloy. The first corresponds to a VED of 69 J/mm^3 (C6), which resulted in the finest microstructure (Figs. 4 and 5) while still achieving a high relative density of over 99.9% (Fig. S2b of the SI). The second condition, with a VED of 167 J/mm^3 (C7), exhibited the highest densification (Fig. S2b of the SI) but also the coarsest and most elongated microstructure (Figs. 4 and 5).

Fig. 7a shows a VLM image of the transition zone between CoCrNi and $(CoCrNi)_{97}Ti_3$ in the AP sample produced at a VED of 69 J/mm^3 (condition C6). Unlike the densification results obtained during the processing parameters evaluation (Fig. S2b of the SI), this larger sample exhibited a notably lower relative density: approximately 95.2% for CoCrNi and 93.8% for $(CoCrNi)_{97}Ti_3$, based on image analysis. This represents a clear example of a size effect, where the larger part size influences the thermal history [49] and, in this case, led to pronounced lack-of-fusion (LoF) defects. As observed in Fig. S2b of the SI, during process parameter optimization with smaller parts, this specific VED condition was already near the threshold below which further reduction in energy density resulted in a significant decrease in relative density. Therefore, when the part size increased, the effective heat input became insufficient, leading to incomplete melting and the formation of LoF defects.

A typical microstructure of the transition zone can be observed in Fig. 7b, where an IPF-Z map along with the corresponding inverse pole figures are presented. As observed, the addition of Ti induced noticeable changes in grain morphology. Distributions of quantitative parameters derived from EBSD analysis are displayed in Figs. 7c to 7e. Notably, the mean equivalent diameter did not decrease with the addition of Ti (Fig. 7c). In fact, the CoCrNi alloy exhibited a slightly smaller average grain size. However, the Ti modification had a pronounced effect on grain morphology, as evidenced by the lower AR in the $(CoCrNi)_{97}Ti_3$ alloy (Fig. 7d), indicating more equiaxed grains. Interestingly, the amount of low-angle grain boundaries (LAGBs, <15°) significantly

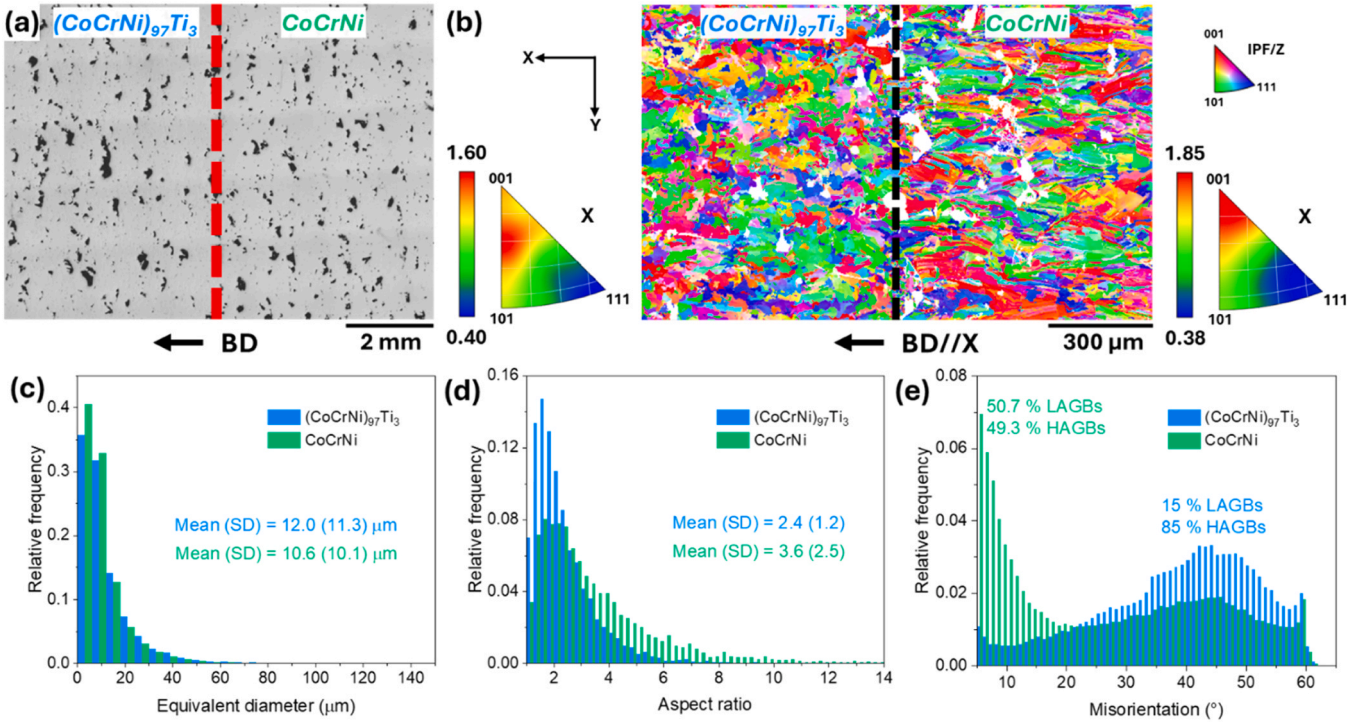

Fig. 7. Transition zone between CoCrNi and $(CoCrNi)_{97}Ti_3$ in the as-printed sample produced at a VED of 69 J/mm^3 (condition C6): (a) VLM image, (b) IPF-Z map with the corresponding inverse pole figures, and distributions derived from EBSD analysis showing (c) equivalent diameter, (d) aspect ratio, and (e) misorientation.

decreased with the compositional modification. This aligns with the absence of substructure formation in $(CoCrNi)_{97}Ti_3$, except in localized Ti-enriched regions (Fig. 3). A similar trend was previously reported in a Ti-modified CoCrFeNi alloy [42]. The observed reduction in AR suggests that Ti addition promoted a transition from columnar to more equiaxed grains. Consequently, the grain boundary character shifted from LAGBs to high-angle grain boundaries (HAGBs) [42]. Columnar grains grow preferentially along the thermal gradient, and during the rapid solidification typical of AM, small misorientations accumulate within the grains, leading to the formation of subgrains separated by LAGBs. This behavior arises from the preferred < 001 > crystallographic orientation during solidification of cubic metals, which largely restricts crystal rotation to a single axis. The resulting reduced randomness in rotation leads to a substantially higher fraction of LAGBs [50]. In contrast,

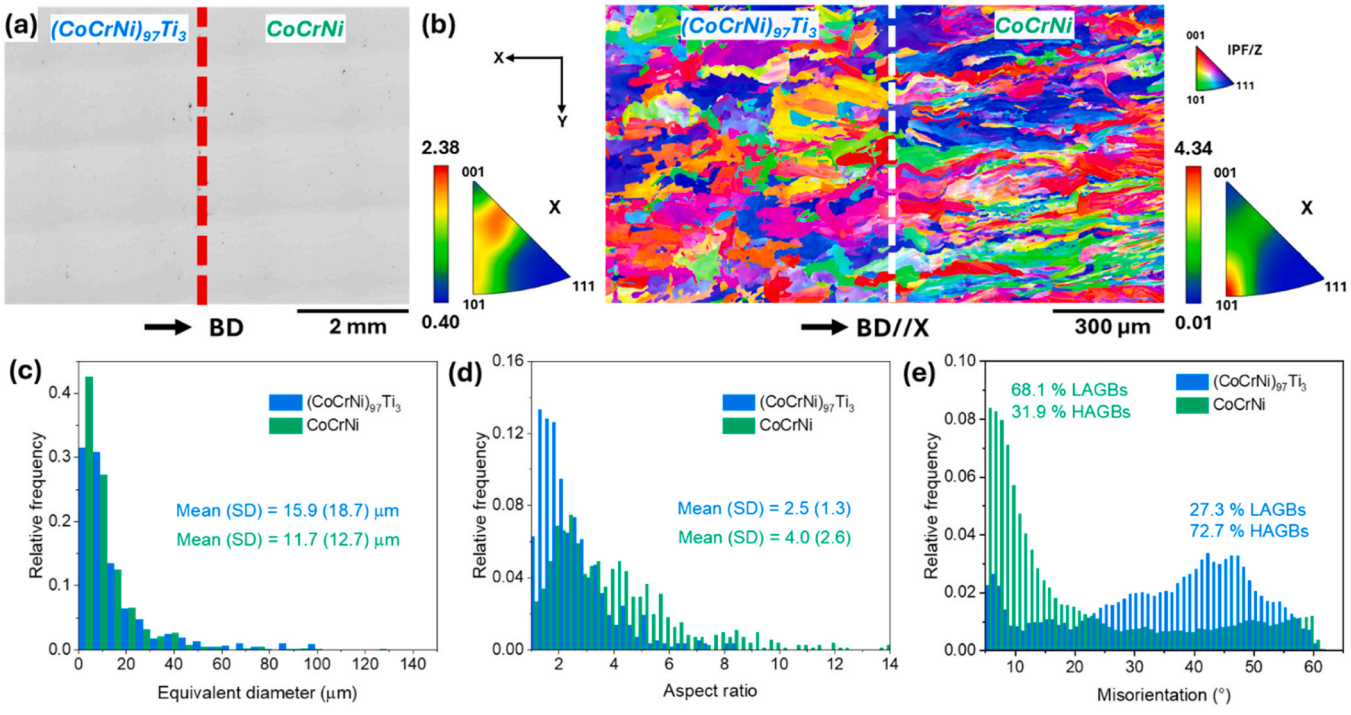

Fig. 8. Transition zone between CoCrNi and $(CoCrNi)_{97}Ti_3$ in the as-printed sample produced at a VED of 167 J/mm^3 (condition C7): (a) VLM image, (b) IPF-Z map with the corresponding inverse pole figures, and distributions derived from EBSD analysis showing (c) equivalent diameter, (d) aspect ratio, and (e) misorientation.

equiaxed grains exhibit a lower fraction of LAGBs because they grow more isotropically and with more random orientations, allowing misorientations to be accommodated at HAGBs rather than accumulating as LAGBs within the grain.

It should be acknowledged that the LoF defects observed in sample C6 may locally alter the melt-pool geometry, thermal gradients, and solidification behavior, potentially introducing bias into EBSD-based grain size and aspect-ratio measurements. Therefore, morphological interpretations drawn from a LoF-dominated region should be treated with caution. Nevertheless, the consistent trends observed in the nearly fully dense $(CoCrNi)_{97}Ti_3$ sample (Figs. 4 and 5) suggest that the influence of LoF defects on grain size and morphology was negligible.

The results for the sample processed with a VED of 167 J/mm^3 (condition C7) are shown in Fig. 8. In this case, high-density samples were successfully produced (Fig. 8a), achieving relative densities above 99.9%, consistent with the parameter optimization process results (Fig. S2b in the SI). A representative microstructure of the transition zone is depicted in Fig. 8b, featuring an IPF-Z map and the corresponding inverse pole figure for each alloy. The general evolution of the microstructure followed a similar trend to that of the C6 condition (Figs. 7b to 7e). Although the higher heat input in this condition resulted in coarser and more elongated grains, as evidenced by the grain size and aspect ratio distributions (Figs. 8c and 8d, respectively), the addition of Ti also influenced grain morphology without promoting refinement. This observation is again corroborated by the lower fraction of LAGBs in the $(CoCrNi)_{97}Ti_3$ alloy (Fig. 8e).

5. Discussion

5.1. Origin of the grain morphological changes

The classical CET mechanism is governed by the interplay between solute effects, arising from constitutional supercooling due to solute buildup ahead of the S/L interface (when the partition coefficient $k < 1$), and thermal effects associated with the thermal gradient (G) and growth rate (R) [47,51]. Under such conditions, CET typically occurs within the laser melt pool from bottom to top as the G/R ratio decreases, leading to a transition from columnar to equiaxed grains as solidification progresses [52]. A complete CET may also occur in alloys with a strong growth-restricting tendency (e.g., elevated Q), which gives rise to a substantially enlarged constitutional supercooling zone and promotes repeated heterogeneous nucleation events during solidification, resulting in the absence of columnar grains [11]. In these cases, the morphological transition is usually accompanied by a reduction in grain size, as a high nucleation rate ahead of the advancing S/L interface is required to fully suppress columnar growth [53].

Ti addition was shown to clearly alter the CoCrNi microstructure by modifying the grain morphology, but without grain size refinement. Moreover, considering the compositional heterogeneity of the samples, regions with more refined grains were not necessarily associated with increased Ti concentrations (Fig. S5 in the SI). This suggests that the observed morphological changes did not originate from the classical CET mechanism. Instead, they likely resulted from local solidification-condition variations associated with the in-situ alloying process. Differences in the physical properties of the constituent powders, such as melting point, thermal conductivity, and absorptivity, combined with complex melting and mixing dynamics, produced local compositional inhomogeneities that influenced the melt pool solidification behavior. These effects altered both the melt pool geometry and the grain growth orientation and morphology, as further evidenced by the distinct texture differences observed upon Ti addition (Figs. 7b and 8b).

During in-situ alloying, the compositional non-uniformity within the liquid implies that the local T_l also varies across the melt pool, influencing nucleation as well as the timing and direction of grain growth [40,54]. While conventional solute pile-up ahead of the solidification front leads to a monotonic increase in T_l, compositional fluctuation fields arising from incomplete mixing and liquid homogenization can locally perturb this behavior. As a result, the liquid ahead of the interface may exhibit either higher or lower T_l relative to the nominal composition, leading to spatially heterogeneous undercooling conditions [55,56]. Accordingly, nucleation may be locally favored or inhibited. Moreover, grain growth uniformity can be affected, as different local compositional variations lead to distinct solidification kinetics, as demonstrated by Shinjo et al. through thermal-chemical-fluid-microstructure modeling of in-situ AM [54]. Such non-uniform nucleation and growth can ultimately disrupt the expected columnar morphology, although it is believed that growth was more affected than nucleation, since if extensive nucleation had occurred, significant grain refinement would have been observed, as demonstrated in recent investigations [55,56]. In this context, the observed change in grain morphology could be ascribed to a CET in a phenomenological sense, although mechanistically it differs from the classical CET.

To explore the proposed hypothesis, results for cast CoCrNi and Ti-modified CoCrNi alloys are presented in Figs. 9a to 9c. It should be noted that an alloy with an even higher Ti concentration was also included to explore a composition with a correspondingly higher Q value (Fig. 1). For the base alloy (Fig. 9a), a fully columnar and coarse-grained microstructure was observed across the analyzed cross-section, regardless of position, either near the Cu mold (Fig. 9a_1) or at the ingot center (Fig. 9a_2). Upon Ti addition, a CET occurred (Figs. 9b and 9c). Near the Cu mold (Figs. 9b_1 and 9c_1), a thin layer of quasi-equiaxed grains formed. However, grains with favorable growth orientations quickly dominated, resulting in a columnar region with much finer grains than those of the Ti-free alloy. These columnar grains continued to grow until conditions such as sufficient constitutional supercooling and a reduced G/R ratio enabled the nucleation of new grains, forming a central equiaxed zone (Figs. 9b_2 and 9c_2). Grain refinement was more pronounced toward the ingot center, with higher Ti content clearly promoting finer grains (mean equivalent diameters of 52 and 34 μm in Figs. 9b_2 and 9c_2, respectively), as expected according to Eqs. 1 and 2.

These findings demonstrate that achieving an equiaxed microstructure during PBF-LB through constitutional supercooling alone is challenging due to the inherently steep thermal gradients, conditions comparable to those near the Cu mold during casting (high G/R ratios). Although this may appear contradictory, since a thin quasi-equiaxed layer is observed in the cast materials, its formation arises because solidification must initiate at the mold wall before directional growth quickly dominates. In contrast, in PBF-LB builds, grains from the previously deposited layer are already available to promote epitaxial growth, strongly favoring the development of columnar microstructures. To validate this interpretation, single-track experiments were performed on the cast samples using the same laser parameters as those employed previously. As exemplified in Figs. 10a to 10c for condition C7 (200 W, 500 mm/s), epitaxial growth was dominant regardless of the condition, inevitably leading to columnar microstructures. This directly supports the previous analysis that the grain morphology differences observed during PBF-LB were primarily driven by compositional inhomogeneities in the melt arising from the in-situ alloying process. This effect may also be a contributing factor to the increasingly columnar nature of the microstructure with rising VED in Fig. 5, as the melt composition became correspondingly more homogeneous.

5.2. Experimental validation of the contribution of Ti to constitutional supercooling

Another important aspect to consider is the effectiveness of Ti in promoting constitutional supercooling, as reflected by the magnitude of Q. As discussed in Section 2, Q was calculated using Eq. 3 and thermodynamic data. Based on this approach, the Q values for CoCrNi, $(CoCrNi)_{97}Ti_3$, and $(CoCrNi)_{94}Ti_6$ were found to be 5.2 °C, 37.5 °C, and 74.1 °C, respectively (Fig. 1). However, thermodynamic predictions rely

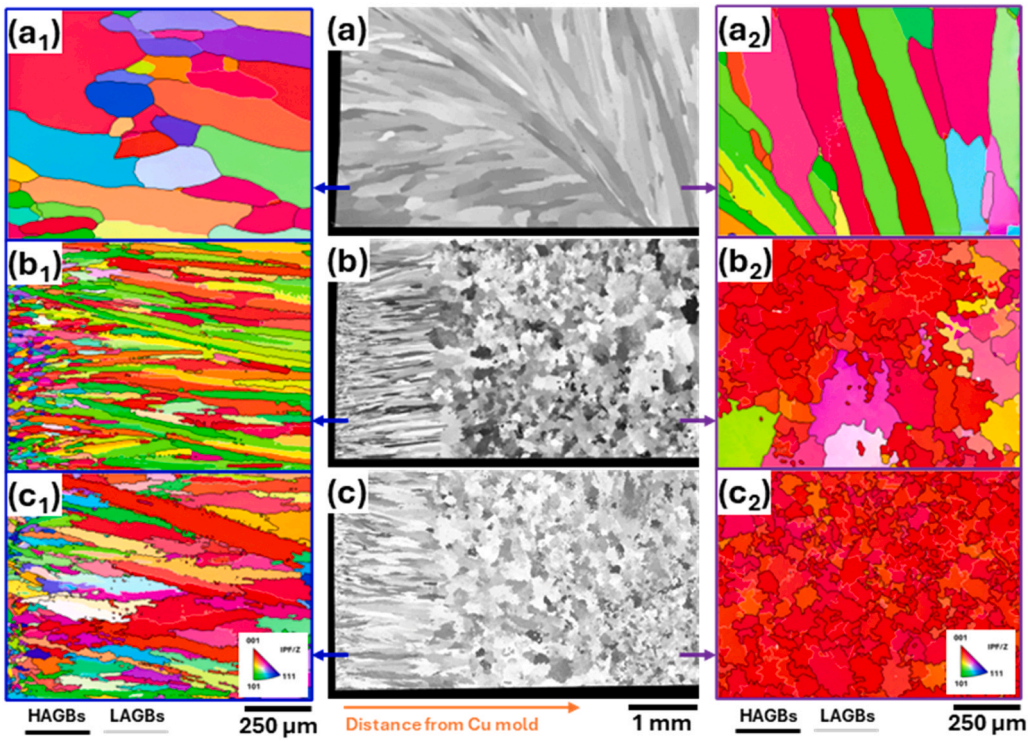

Fig. 9. Microstructural analysis (BSE-SEM images and EBSD maps) of cross-sections of cast ingots: (a) CoCrNi, (b) $(CoCrNi)_{97}Ti_3$, and (c) $(CoCrNi)_{94}Ti_6$. The EBSD results show microstructures near the Cu mold surface (a_1, b_1, c_1) and at the ingot center (a_2, b_2, c_2).

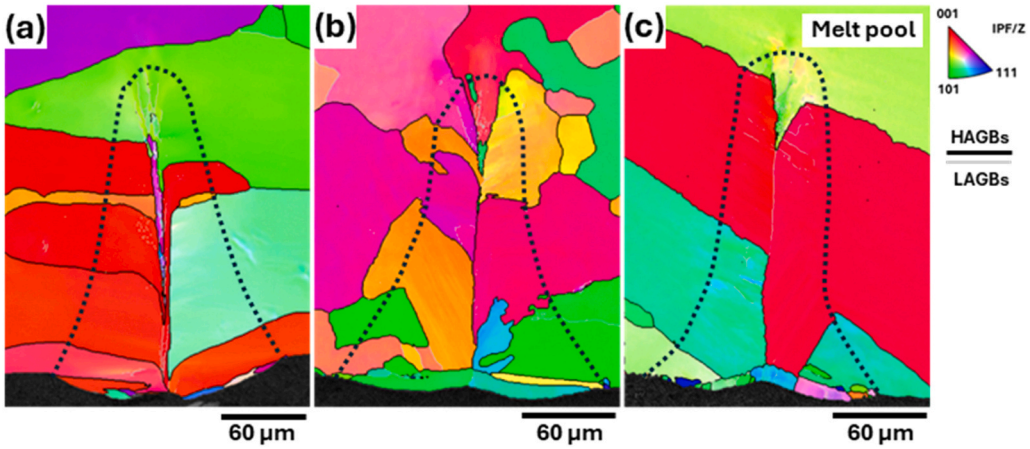

Fig. 10. EBSD maps showing the microstructure of laser-processed single-tracks (200 W, 500 mm/s) on cast ingots of: (a) CoCrNi, (b) $(CoCrNi)_{97}Ti_3$, and (c) $(CoCrNi)_{94}Ti_6$.

on database accuracy, which must be properly validated. To address this, experimental verification was carried out through thermal analysis. It is worth noting that although Q was derived from non-equilibrium Scheil solidification curves, using equilibrium solidification curves instead would yield identical results, since the slope of the ΔT_{CS}—f_s curve in the limit $f_s \rightarrow 0$ is rigorously the same under these two conditions [31]. DSC, widely employed for determining *liquidus* and *solidus* temperatures and for benchmarking thermodynamic phase diagram predictions in metallic systems [57,58], therefore represents an appropriate tool for experimental estimation of Q.

Figs. 11a and 11b present two DSC cycles, corresponding to the heating and cooling scans of the $(CoCrNi)_{97}Ti_3$ AP sample, respectively. Notably, significant differences were observed between the first and second heating scans (Fig. 11a), primarily due to compositional inhomogeneities in the printed material. These inhomogeneities even led to isolated melting events, highlighted by the dashed contour in Fig. 11a. During the first heating cycle, after melting, compositional homogenization occurred within the DSC furnace, which explains why the subsequent cooling scans exhibited more consistent behavior (Fig. 11b). Nonetheless, some variation in transformation temperatures remained, due to undercooling effects.

Due to the small mass of the DSC samples, some deviation from the nominal composition may be expected for the AP material after compositional homogenization during the first melting cycle inside the DSC furnace. Therefore, the cast samples, which present a more homogeneous overall composition, were used for the determination of the experimental *liquidus* and *solidus* temperatures. The second heating data were selected to avoid the influences of undercooling, and the same experimental procedure was applied to the CoCrNi and $(CoCrNi)_{94}Ti_6$ alloys. The *solidus* temperature was taken as the temperature

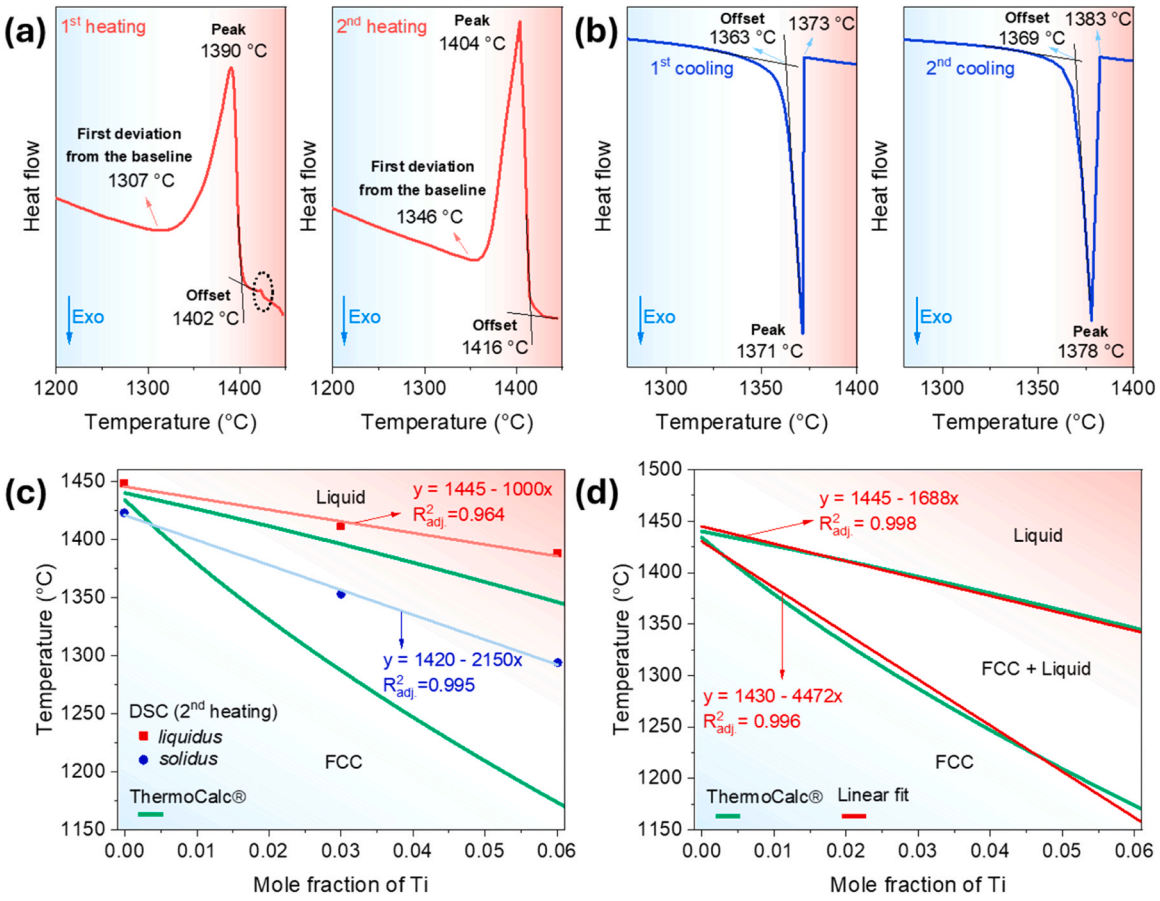

Fig. 11. DSC results and comparison with thermodynamic calculations: (a,b) first and second heating and cooling cycles showing the melting and solidification behavior of the as-printed $(CoCrNi)_{97}Ti_3$ alloy, (c) experimentally determined *liquidus* and *solidus* temperatures for CoCrNi, $(CoCrNi)_{97}Ti_3$, and $(CoCrNi)_{94}Ti_6$ alloys, assuming linear phase boundaries, and (d) linear approximations of thermodynamically calculated phase boundaries.

corresponding to the first deviation from the baseline, which represents the onset of melting and is thus considered the most reliable estimate of the *solidus* temperature [59,60]. The first deviation was determined using the derivative method [61]. In the case of the *liquidus*, the peak temperature of the final thermal event was regarded as the *liquidus* temperature [59,61–64]. The experimentally measured values were then compared with those obtained from thermodynamic calculations, as shown in Fig. 11c. Notably, discrepancies were observed, and these increased with increasing Ti content (Table 1). For the CoCrNi alloy, the measured solidification interval was larger than the calculated one, whereas the Ti-modified alloys exhibited the opposite trend. Regardless of composition, the deviation in the *solidus* temperature was more pronounced than that observed for the *liquidus*.

To calculate the experimental Q, the *liquidus* and *solidus* lines were assumed to be linear, as illustrated in Fig. 11c, and the following equation was applied [65]:

$$Q = m_l C_0 \left(\frac{m_l}{m_s} + \frac{\Delta T_{M0}}{m_s C_0} - 1 \right) \quad (4)$$

where m_s is slope of the *solidus* line, and ΔT_{M0} is the solidification interval of the base alloy. Using this methodology, the experimentally determined Q was 11.6 °C for CoCrNi, 27.7 for $(CoCrNi)_{97}Ti_3$, and 43.7 °C for $(CoCrNi)_{94}Ti_6$. When the same Eq. 4 was applied to the thermodynamic data, also assuming linear *liquidus* and *solidus* lines as shown in Fig. 11d, the calculated Q was 5.7 °C for CoCrNi, 37.2 °C for $(CoCrNi)_{97}Ti_3$, and 68.7 °C for $(CoCrNi)_{94}Ti_6$, which are consistent with the results obtained using Eq. 3. These findings demonstrate that the effectiveness of Ti in promoting constitutional supercooling is lower than initially predicted by thermodynamic modeling. Based on the assumption of linear phase boundaries, which is supported by the quality of the linear fits (high adjusted coefficients of determination in Figs. 11c and 11d), the calculated Q_{Ti} per atomic unit is 10.5 °C, whereas the experimentally determined Q_{Ti} per atomic unit is roughly half this value, about 5.4 °C. This discrepancy highlights the importance of experimental validation of thermodynamic databases, particularly for multicomponent alloys, as inaccuracies can mislead alloy design strategies and the interpretation of experimental results.

Table 1
Comparison of l*iquidus* and *solidus* temperatures obtained from thermodynamic calculations and experimental measurements.

Alloy	*Liquidus* (°C)		Temperature deviation (°C)	*Solidus* (°C)		Temperature deviation (°C)
	Calculated	Measured		Calculated	Measured	
CoCrNi	1440	1447	−7	1434	1422	12
$(CoCrNi)_{97}Ti_3$	1396	1410	−14	1287	1352	−65
$(CoCrNi)_{94}Ti_6$	1346	1387	−41	1174	1293	−119

5.3. Segregation behavior

The extent of segregation varies significantly with the solidification regime. At sufficiently high solidification velocities, a reduction in segregation is observed. This behavior reflects the phenomenon of solute trapping, which occurs when the interface growth velocity approaches or exceeds the atomic diffusion rate. Under such rapid solidification conditions, solute trapping may become so pronounced that partitionless solidification takes place [66–68], meaning the solid forms with the same composition as the liquid, without microsegregation. In the absence of partitioning, growth restriction is effectively eliminated [69]. In this context, partitionless solidification has already been assumed to occur during PBF-LB of the CoCrNi alloy [9].

Fig. 12a illustrates the elemental segregation behavior within the primary FCC phase of $(CoCrNi)_{97}Ti_3$, as predicted by the Scheil model. For comparison, Fig. 12b shows the DSC heating curve of the as-cast alloy, where two distinct melting peaks can be observed, unlike the results shown in Fig. 11a for the AP sample. These peaks correspond to the melting of compositionally distinct regions, a direct consequence of elemental segregation during solidification. Specifically, dendritic and interdendritic regions differ in composition and, therefore, melt at dissimilar temperatures.

Fig. 12c displays a Ti SEM-EDS map from the single-track laser experiment. In the as-cast region, strong Ti segregation to interdendritic

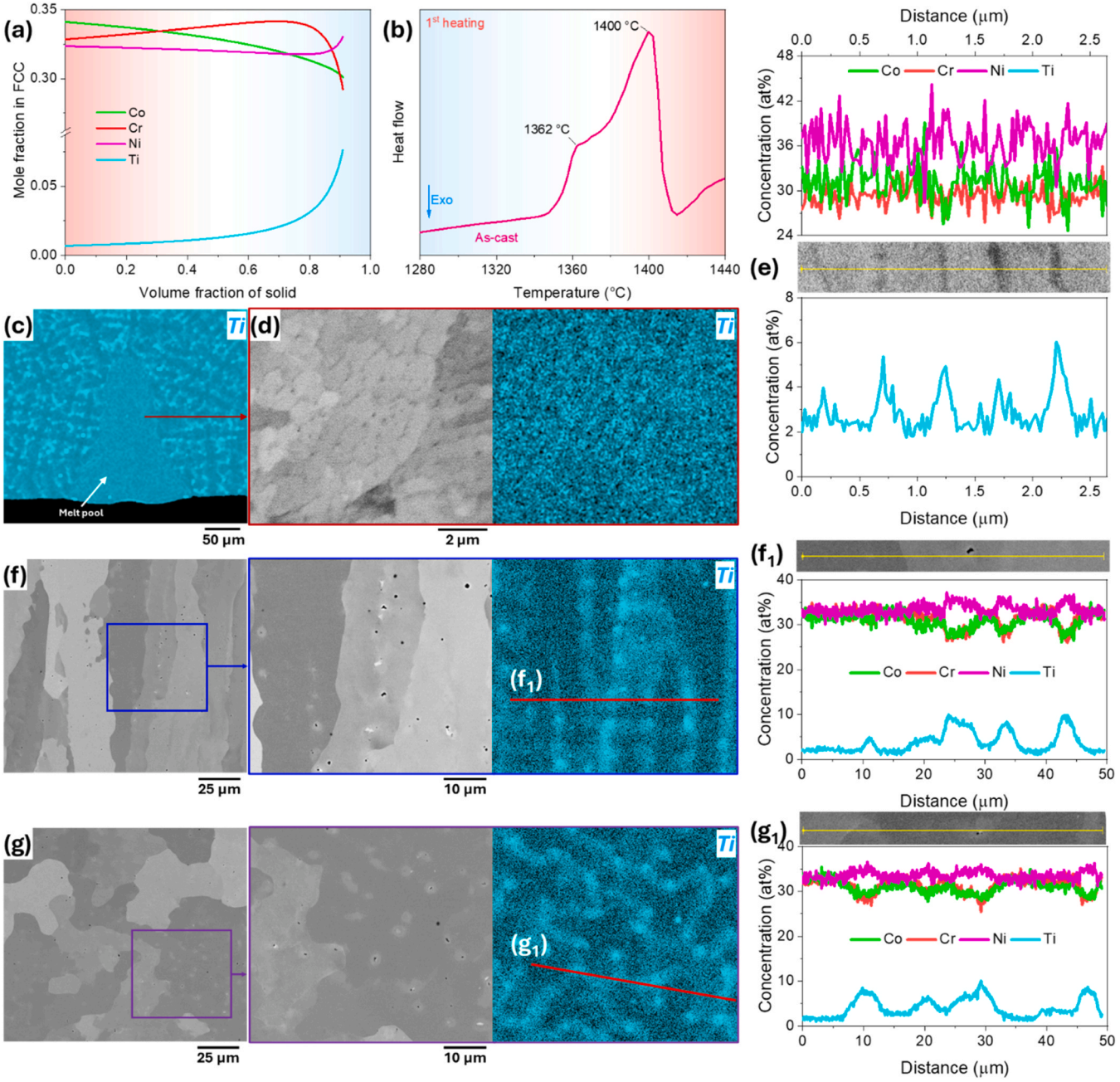

Fig. 12. Segregation analysis of the $(CoCrNi)_{97}Ti_3$ alloy: (a) Scheil solidification curve predicting elemental segregation in the primary FCC phase; (b) DSC heating curve of the as-cast sample; (c) Ti EDS map from a single-track laser experiment; (d) BSE-SEM image with the corresponding Ti EDS map of the melt pool region; (e) typical EDS line scan across the melt pool region; (f) BSE-SEM images with the corresponding Ti EDS map of the as-cast alloy near the Cu mold surface; (f_1) EDS line scan along the line highlighted in (f); (g) BSE-SEM images with the corresponding Ti EDS map of the as-cast alloy at the ingot center; and (g_1) EDS line scan along the line highlighted in (g).

areas is evident, consistent with the Scheil prediction (Fig. 12a). In contrast, the laser-processed zone appears more compositionally uniform, suggesting a tendency toward partitionless solidification. However, higher magnification BSE-SEM imaging (Fig. 12d) reveals that segregation still occurred. Ti-rich regions are clearly visible in the BSE image, although they are not well resolved in the corresponding EDS map. An EDS line scan shown in Fig. 12e confirms this, showing Ti concentrations up to ~6 at%. Additional analyses in the as-cast alloy, near both the Cu mold surface and the ingot center (Figs. 12f and 12g), revealed similar segregation behavior: Ti and Ni enriched in interdendritic regions, while Co and Cr were depleted, in agreement with the Scheil prediction (Fig. 12a). Notably, Ti segregation reached up to ~10 at%, and the partitioning of the other elements was also more pronounced (Figs. 12f_1 and 12g_1), in contrast with the laser-processed sample (Fig. 12e). This trend is corroborated by BSE contrast: in the laser-processed region, Ti-rich interdendritic regions appear darker (Figs. 12d and 12e), whereas in the as-cast samples, Ti-rich regions appear brighter due to their higher Ni contents (Figs. 12f and 12g).

The DSC and microstructural characterization results confirm that the extent of segregation depends on the solidification velocity, as expected [70]. Although solidification during single-track laser processing did not reach the partitionless regime, the rapid solidification reduced solute segregation compared to casting. Indeed, in Ti-poor regions of the PBF-LB sample, no evidence of segregation was detected (Fig. 3c). This observation can be attributed to the combined effect of rapid solidification and local solute concentration. Under the rapid solidification conditions characteristic of PBF-LB, solute trapping partially modifies partitioning, thereby reducing the extent of segregation. In Ti-poor regions (Fig. 3c), the combination of low Ti content and reduced partitioning leads to segregation levels that are below the detection limit of the characterization technique. In contrast, in Ti-rich regions (Fig. 3f), the higher local solute concentration promotes measurable solute rejection during solidification, resulting in Ti enrichment along cellular boundaries.

This behavior implies that the effective partition coefficient (k_v) is higher during laser processing than under casting conditions, leading to a correspondingly reduced effective Q (Q_v) in the laser-processed material. To estimate k_v, the continuous growth model (CGM) developed by Aziz was applied [71–73]:

$$k_v = \frac{\left(k + \frac{a_0 v}{D_i}\right)}{\left(1 + \frac{a_0 v}{D_i}\right)} \tag{5}$$

where a_0 is the atomic jump distance, v is the interface growth velocity, and D_i is the solute diffusion coefficient at the S/L interface. The nearest-neighbor distance of the FCC structure was used as an approximation for a_0, yielding $a_0 = 2.59 \times 10^{-10}$ m, based on Thermo-Calc® predictions of the average lattice parameter in the solidification range. The interface velocity was approximated by the laser scan speed [73], which represents an upper-bound estimate under PBF-LB conditions. Because D_i is difficult to determine experimentally, the solute diffusion in liquid (D) is commonly taken as an approximation [73,74]. For the $(CoCrNi)_{97}Ti_3$ alloy, Fig. 13a shows the influence of v on k_v for several values of D, while the corresponding effect on Q_v is presented in Fig. 13b. Eq. 2 was used to calculate Q_v, replacing k with k_v and m_l with the velocity-dependent *liquidus* slope (m_v). The latter was determined using [72]:

$$m_v = m_l \frac{1 - k_v + k_v \ln\left(\frac{k_v}{k}\right)}{(1 - k)} \tag{6}$$

The equilibrium k (k_e) was obtained from the DSC results (Fig. 11c) and calculated by applying [65]:

$$k_e = \frac{m_l C_0 + \Delta T_{M0}}{m_s C_0} \tag{7}$$

which yields $k_e = 0.078$. Since k_e changes during the progression of solidification (Fig. 11c), the value of k_e considered in Eq. 7 corresponds to the beginning of solidification, which is most appropriate given the physical meaning of Q, as it is defined at the onset of solidification [65].

Fig. 13a shows that solute trapping is expected to occur within the typical v range employed in PBF-LB. However, partitionless solidification would require velocities far higher than those achievable in the process, which is consistent with the experimental observations. Considering that the liquid diffusion coefficients of the constituent elements of this alloy typically fall in the range of 1–5 $\times$ 10^{-9} m^2/s [53,74,75], the corresponding Q_v ranges from 25.9 °C to 27.1 °C. This suggests that solute trapping has only a minor effect under the present processing conditions, even under this conservative upper-bound estimate of the interface velocity.

5.4. Implications of the Q parameter for grain refining efficiency in PBF-LB

Although increasing Q has been widely employed as a strategy to promote grain refinement in PBF-LB [76–78], a recent study by Brooke et al. [73] demonstrated that, under the high solidification velocity characteristic of AM processes, the dendrite tip undercooling correlates more closely with the constitutional supercooling parameter P than with Q. This finding suggests that the total constitutional supercooling available (P) could be a better indicator of grain refining efficiency in

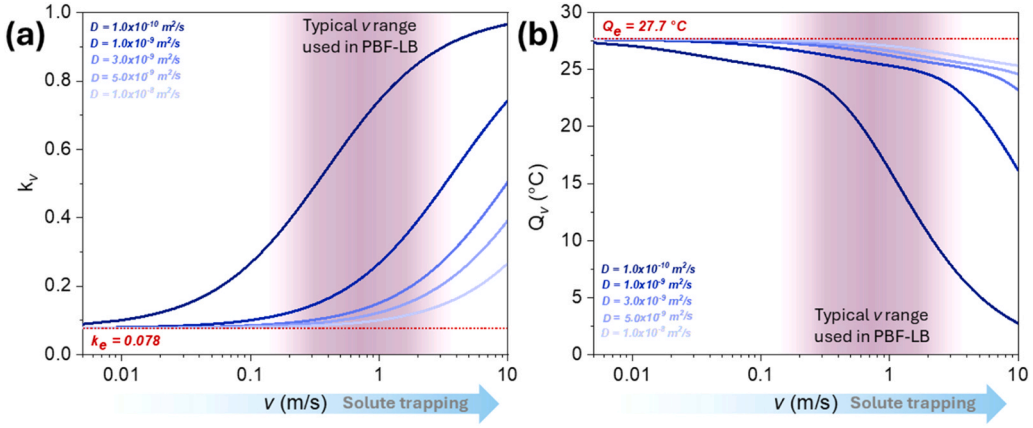

Fig. 13. Solute trapping in the $(CoCrNi)_{97}Ti_3$ alloy: variation of the effective (a) partition coefficient (k_v) and (b) growth restriction factor (Q_v) with laser scan speed (v) for different solute diffusion coefficients in the liquid (D).

PBF-LB than the rate of development of constitutional supercooling (Q). This distinction is particularly important in cases where an alloy exhibits a high Q but a low P, a condition that still favors the formation of columnar microstructures despite the elevated Q [73]. This is not the case here, however, as the addition of Ti led to simultaneous increases in both Q and P.

The same procedure used to calculate the experimental Q values from the DSC data (Fig. 11c) was also applied to determine P, using the following equation [65]:

$$P = m_l C_0 - m_s C_0 + \Delta T_{M0} \quad (8)$$

P increased from 35 °C for CoCrNi to 58 °C for $(CoCrNi)_{97}Ti_3$. Again, based on the thermodynamic data, this increase was much more pronounced, from approximately 6 °C to 109 °C.

During alloy design, it must be recognized that the Q values required to promote a CET depend strongly on the processing route. Accordingly, the critical Q for CET increases with increasing solidification velocity. Moreover, under high solidification velocity regimes, additional alloy parameters must be considered when assessing grain refinement efficiency [73]. Among the typical metal AM processes, PBF-LB exhibits the highest thermal gradients [73,79]. Consequently, the Q values required to promote a CET are also expected to be higher in alloys processed by PBF-LB compared with other AM processes. In the specific case of CoCrNi, further increasing in Q through alloying additions is challenging without promoting the formation of secondary phases, such as the σ phase shown in Fig. S4, which may compromise its otherwise favorable mechanical performance.

The steep thermal gradients inherent to PBF-LB processing, on the order of 10^5 - 10^7 °C/m [26,80], may limit the effectiveness of solute additions in promoting CET in CoCrNi by reducing the spatial extent of the constitutionally supercooled region ahead of the S/L interface [81]. Nevertheless, successful grain refinement using this strategy has been reported in the literature for other alloy systems [76–78]. A notable example is the study by Zhai et al. [76], in which Ti was added to 316 L stainless steel via in-situ alloying, resulting in significant grain refinement without the use or presence of effective inoculants. A strong correlation between grain size and the Q parameter was observed, aligning well with Eq. 1. Moreover, grain refinement was achieved even with Q values lower ($\leq$ 20 °C) than those explored in the present study, suggesting that the nucleation in 316 L is more favorable than in CoCrNi. This may be attributed to a shorter incubation time or a lower energy barrier, facilitating solid-phase nucleation [26]. Although 316 L stainless steel exhibits an FCC microstructure at room temperature, it solidifies through a body-centered cubic (BCC) phase, which typically has a lower solid-liquid interfacial free energy, thereby reducing the nucleation barrier during solidification [81,82]. This could indicate that BCC structures are more prone to grain refinement via solute additions under PBF-LB processing conditions. Accordingly, the Q threshold required to achieve equiaxed grains is also highly alloy dependent.

Recent studies [25,26] have shown that, under rapid solidification conditions, the role of solutes in grain refinement may be more strongly associated with the generation of large thermal undercooling ahead of the S/L interface rather than solely with constitutional supercooling effects described by Q. Solute rejection during solidification can retard the effective advancement of the S/L interface relative to the liquidus isotherm, leading to an increase in local thermal undercooling. This enhanced undercooling may significantly increase the activation frequency of heterogeneous nucleation events, thus improving grain refinement efficiency regardless of the Q value [26]. These observations, together with the findings of the present investigation, indicate that although Q remains a simple alloy design parameter, it may not be sufficient to fully describe grain refinement efficiency under PBF-LB conditions. The rapid solidification effects, particularly those associated with interface kinetics, solute redistribution, and thermal undercooling, should also be considered. Accordingly, the present results suggest that grain refinement in PBF-LB should be interpreted through a combination of constitutional effects, growth kinetics, and nucleation behavior, rather than through classical casting-based theories alone. Therefore, future studies should aim to establish more comprehensive solidification frameworks integrating thermodynamic and kinetic effects to improve alloy design strategies for PBF-LB.

6. Summary and conclusions

This work evaluated the effectiveness of solute-driven constitutional supercooling for grain refinement in CoCrNi-based MEAs processed by PBF-LB, using Ti as a model solute. Although thermodynamic calculations predicted a strong growth-restricting effect of Ti, the addition of 3 at% Ti did not lead to grain size refinement. Instead, Ti primarily modified the grain morphology, disrupting columnar growth and promoting more equiaxed grains without inducing a classical CET. This morphological change was attributed to in-situ alloying effects, particularly differences in the physical properties and melting behavior of the constituent powders, which altered melt pool dynamics and solidification behavior.

Experimental thermal analysis further revealed that thermodynamic predictions overestimated Q of Ti in CoCrNi, emphasizing the need for experimental validation of solute selection strategies in multicomponent alloys.

Although rapid solidification during PBF-LB reduced solute segregation compared to casting, fully partitionless solidification was not achieved. Solute trapping still contributed to a reduction in the effective Q. However, this reduction was limited and therefore could not be considered a major factor in the limited effectiveness of grain refinement.

Overall, these results demonstrate that increasing Q through solute addition alone may be insufficient to achieve grain refinement in alloys processed by PBF-LB. The steep thermal gradients and high solidification velocities inherent to this process limit the ability of solute-driven constitutional supercooling to promote grain refinement, such that the critical values of Q required to promote a CET may exceed those attainable without inducing secondary phase formation. Consequently, the process-specific solidification conditions in PBF-LB dominate microstructural evolution in CoCrNi alloys. This emphasizes the importance of coupling alloy design with process optimization and complementary grain refinement strategies to achieve microstructural control in PBF-LB-processed CoCrNi alloys.

CRediT authorship contribution statement

Ameer Hamza Khan: Investigation, Formal analysis, Visualization, Writing – Review & Editing. **Sri Bala Aditya Malladi:** Investigation, Formal analysis. **Marcio Sangali Cristino da Silva:** Investigation. **João Felipe Queiroz Rodrigues:** Investigation, Writing – Review & Editing. **Sheng Guo:** Conceptualization, Validation, Resources, Writing – Review & Editing. **Kaio Niitsu Campo:** Conceptualization, Investigation, Validation, Visualization, Supervision, Funding acquisition, Writing – Original Draft.

Declaration of Competing Interest

The authors declare that they have no known competing financial interests or personal relationships that could have appeared to influence the work reported in this paper.

Acknowledgments

The authors gratefully acknowledge the Brazilian research funding agencies for their financial support: CAPES (Coordination for the Improvement of Higher Education Personnel, Grant No. 88887.974930/2024–00), and FAPESP (São Paulo Research Foundation, Grants No. 2018/18293–8, 2024/02618–6, and 2024/22719–1). The authors also

thank the Brazilian Nanotechnology National Laboratory (LME/LNNano/CNPEM) for providing access to the SEM/FIB/TEM facilities (Proposals IDs: 20242988 and 20243058), and Prof. Rubens Caram for granting access to his laboratory. The Article Processing Charge (APC) for this publication was funded by the Coordination for the Improvement of Higher Education Personnel - CAPES (ROR: 00x0ma614). For open access purposes, the authors have assigned a Creative Commons CC BY license to any accepted version of the article.

Appendix A. Supporting information

Supplementary data associated with this article can be found in the online version at doi:10.1016/j.addma.2026.105279.

Data availability

Data will be made available on request.

References

[1] G. Laplanche, A. Kostka, C. Reinhart, J. Hunfeld, F. Eggeler, E.P. George, Reasons for the superior mechanical properties of medium-entropy CrCoNi compared to high-entropy CrMnFeCoNi, Acta Mater. 128 (2017) 292–303, https://doi.org/10.1016/j.actamat.2017.02.036.

[2] J. Wang, W. Li, H. Yang, H. Huang, S. Ji, J. Ruan, Z. Liu, Corrosion behavior of CoCrNi medium-entropy alloy compared with 304 stainless steel in H_2SO_4 and NaOH solutions, Corros. Sci. 177 (2020) 108973, https://doi.org/10.1016/j.corsci.2020.108973.

[3] M.P. Agustianingrum, U. Lee, N. Park, High-temperature oxidation behaviour of CoCrNi medium-entropy alloy, Corros. Sci. 173 (2020) 108755, https://doi.org/10.1016/j.corsci.2020.108755.

[4] S. Bajpai, B.E. MacDonald, T.J. Rupert, H. Hahn, E.J. Lavernia, D. Apelian, Recent progress in the CoCrNi alloy system, Materialia 24 (2022) 101476, https://doi.org/10.1016/j.mtla.2022.101476.

[5] H. He, Y. Wang, Y. Qi, Z. Xu, Y. Li, Review on the preparation methods and strengthening mechanisms of medium-entropy alloys with CoCrNi as the main focus, J. Mater. Res. Technol. 27 (2023) 6275–6307, https://doi.org/10.1016/j.jmrt.2023.10.266.

[6] F. Weng, Y. Chew, Z. Zhu, X. Yao, L. Wang, F.L. Ng, S. Liu, G. Bi, Excellent combination of strength and ductility of CoCrNi medium entropy alloy fabricated by laser aided additive manufacturing, Addit. Manuf. 34 (2020) 101202, https://doi.org/10.1016/j.addma.2020.101202.

[7] P. Niu, R. Li, K. Gan, T. Yuan, S. Xie, C. Chen, Microstructure, properties, and metallurgical defects of an equimolar CoCrNi medium entropy alloy additively manufactured by selective laser melting, Metall. Mater. Trans. A 52 (2021) 753–766, https://doi.org/10.1007/s11661-020-06121-4.

[8] X. Bi, R. Li, T. Li, C. Wang, Z. Yuan, J. Cheng, Improvement of mechanical properties at cryogenic temperature of CoCrNi medium entropy alloy fabricated by hybrid additive manufacturing technology, Mater. Charact. 205 (2023) 113351, https://doi.org/10.1016/j.matchar.2023.113351.

[9] J. Ge, C. Chen, R. Zhao, Q. Liu, Y. Long, J. Wang, Z. Ren, S. Yin, Strength-ductility synergy of CoCrNi medium-entropy alloy processed with laser powder bed fusion, Mater. Des. 219 (2022) 110774, https://doi.org/10.1016/j.matdes.2022.110774.

[10] C. Li, M. Jain, Q. Liu, Z. Cao, M. Ferry, J.J. Kruzic, B. Gludovatz, X. Li, Multi-scale microstructure manipulation of an additively manufactured CoCrNi medium entropy alloy for superior mechanical properties and tunable mechanical anisotropy, Addit. Manuf. 84 (2024) 104104, https://doi.org/10.1016/j.addma.2024.104104.

[11] D. Zhang, D. Qiu, M.A. Gibson, Y. Zheng, H.L. Fraser, D.H. StJohn, M.A. Easton, Additive manufacturing of ultrafine-grained high-strength titanium alloys, Nature 576 (2019) 91–95, https://doi.org/10.1038/s41586-019-1783-1.

[12] J. Günther, F. Branne, M. Droste, M. Wendler, O. Volkova, H. Biermann, T. Niendorf, Design of novel materials for additive manufacturing - Isotropic microstructure and high defect tolerance, Sci. Rep. 8 (2018) 1298, https://doi.org/10.1038/s41598-018-19376-0.

[13] Y. Kok, X.P. Tan, P. Wang, M.L.S. Nai, N.H. Loh, E. Liu, S.B. Tor, Anisotropy and heterogeneity of microstructure and mechanical properties in metal additive manufacturing: A critical review, Mater. Des. 139 (2018) 565–586, https://doi.org/10.1016/j.matdes.2017.11.021.

[14] Y. Yehorov, L.J. da Silva, A. Scotti, Exploring the use of switchback for mitigating homoepitaxial unidirectional grain growth and porosity in WAAM of aluminium alloys, Int. J. Adv. Manuf. Technol. 104 (2019) 1581–1592, https://doi.org/10.1007/s00170-019-03959-w.

[15] W. Huang, X. Chen, X. Huang, H. Wang, Y. Zhu, Anisotropic study of Ti6Al4V alloy formed by selective laser melting, JOM 73 (2021) 3804–3811, https://doi.org/10.1007/s11837-021-04765-0.

[16] Z. Yang, L. Zhu, J. Ning, S. Wang, P. Xue, P. Xu, Y. Dun, B. Xin, G. Zhang, Revealing the influence of ultrasound/heat treatment on microstructure evolution and tensile failure behavior in 3D-printing of Inconel 718, J. Mater. Process. Technol. 305 (2022) 117574, https://doi.org/10.1016/j.jmatprotec.2022.117574.

[17] F. Zhou, X. Hu, Y. Zhou, Z. Xu, C. Guo, G. Li, Z. Li, Y. Huang, Q. Zhu, Effects of post-heat treatment on anisotropic mechanical properties of laser additively manufactured IN718, Mater. Sci. Eng. A 877 (2023) 145144, https://doi.org/10.1016/j.msea.2023.145144.

[18] C. Pan, D. Zhu, H. Luo, K. Kosiba, S. Qu, C. Yang, X. Li, Fabrication of high-performance CoCrNi medium entropy alloy by laser powder bed fusion: The effect of grain boundary segregation, Compos. B Eng. 253 (2023) 110540, https://doi.org/10.1016/j.compositesb.2023.110540.

[19] G. Li, E. Brodu, J. Soete, H. Wei, T. Liu, T. Yang, W. Liao, K. Vanmeensel, Exploiting the rapid solidification potential of laser powder bed fusion in high strength and crack-free Al-Cu-Mg-Mn-Zr alloys, Addit. Manufac 47 (2021) 102210, https://doi.org/10.1016/j.addma.2021.102210.

[20] S. Kou, A criterion for cracking during solidification, Acta Mater. 88 (2015) 366–374, https://doi.org/10.1016/j.actamat.2015.01.034.

[21] M. Opprecht, J.-P. Garandet, G. Roux, C. Flament, M. Soulier, A solution to the hot cracking problem for aluminium alloys manufactured by laser beam melting, Acta Mater. 197 (2020) 40–53, https://doi.org/10.1016/j.actamat.2020.07.015.

[22] Q. Tan, J. Zhang, Q. Sun, Z. Fan, G. Li, Y. Yin, Y. Liu, M.-X. Zhang, Inoculation treatment of an additively manufactured 2024 aluminium alloy with titanium nanoparticles, Acta Mater. 196 (2020) 1–16, https://doi.org/10.1016/j.actamat.2020.06.026.

[23] V.P.N. Samy, M. Schäfle, F. Brasche, U. Krupp, C. Haase, Understanding the mechanisms of columnar-to-equiaxed transition and grain refinement in additively manufactured steel during laser powder bed fusion, Addit. Manuf. 73 (2023) 103702, https://doi.org/10.1016/j.addma.2023.103702.

[24] X. Zhu, Z. Zhu, T. Liu, W. Liao, Y. Du, H. Wei, Crack-free and high-strength AA2024 alloy obtained by additive manufacturing with controlled columnar-equiaxed-transition, J. Mater. Sci. Technol. 156 (2023) 183–196, https://doi.org/10.1016/j.jmst.2023.01.012.

[25] A. Prasad, L. Yuan, P. Lee, M. Patel, D. Qiu, M. Easton, D. StJohn, Towards understanding grain nucleation under additive manufacturing solidification conditions, Acta Mater. 195 (2020) 392–403, https://doi.org/10.1016/j.actamat.2020.05.012.

[26] Q. Tan, Y. Yin, A. Prasad, G. Li, Q. Zhu, D.H. StJohn, M.-X. Zhang, Demonstrating the roles of solute and nucleant in grain refinement of additively manufactured aluminum alloys, Addit. Manuf. 49 (2022) 102516, https://doi.org/10.1016/j.addma.2021.102516.

[27] Z. Fan, Q. Tan, L. Yuan, X. Li, Y. Yin, P. Niu, Y. Zhao, C. Kang, R. Li, T. Yuan, D. H. StJohn, M.-X. Zhang, H. Huang, Solute-induced grain refinement for crack suppression in laser additive manufactured ceramics, Acta Mater. 292 (2025) 121069, https://doi.org/10.1016/j.actamat.2025.121069.

[28] D.H. StJohn, M. Qian, M.A. Easton, P. Cao, The Interdependence Theory: The relationship between grain formation and nucleant selection, Acta Mater. 59 (2011) 4907–4921, https://doi.org/10.1016/j.actamat.2011.04.035.

[29] M.A. Easton, D.H. StJohn, A model of grain refinement incorporating alloy constitution and potency of heterogeneous nucleant particles, Acta Mater. 49 (2001) 1867–1878, https://doi.org/10.1016/S1359-6454(00)00368-2.

[30] J.-O. Andersson, T. Helander, L. Höglund, P. Shi, B. Sundman, Thermo-Calc & DICTRA, computational tools for materials science, Calphad 26 (2002) 273–312, https://doi.org/10.1016/S0364-5916(02)00037-8.

[31] R. Schmid-Fetzer, A. Kozlov, Thermodynamic aspects of grain growth restriction in multicomponent alloy solidification, Acta Mater. 59 (2011) 6133–6144, https://doi.org/10.1016/j.actamat.2011.06.026.

[32] W.-C. Chang, C.-H. Hsueh, Strengthening of CoCrNi medium entropy alloy with Ti additions, Intermetallics 163 (2023) 108072, https://doi.org/10.1016/j.intermet.2023.108072.

[33] P.-K. Shen, H.-C. Liu, C.-Y. Huang, H.-W. Yen, J.-W. Yeh, C.-W. Tsai, Microstructure and mechanical properties of medium-entropy alloys with a high-density η-$D0_{24}$ phase, Mater. Charact. 185 (2022) 111713, https://doi.org/10.1016/j.matchar.2021.111713.

[34] M. Sangali, J.F.Q. Rodrigues, K.N. Campo, L.F. Starck, A. Cremasco, R.J. Contieri, R. Caram, Fine-layered CP-Ti/Ti-6Al-4V composites by laser powder bed fusion, Vacuum 220 (2024) 112831, https://doi.org/10.1016/j.vacuum.2023.112831.

[35] M.H. Mosallanejad, B. Niroumand, A. Aversa, A. Saboori, In-situ alloying in laser-based additive manufacturing processes: A critical review, J. Alloy. Compd. 872 (2021) 159567, https://doi.org/10.1016/j.jallcom.2021.159567.

[36] R.E. Bedford, G. Bonnier, H. Maas, F. Pavese, Recommended values of temperature on the international temperature scale of 1990 for a selected set of secondary reference points, Metrologia 33 (1996) 133–154, https://doi.org/10.1088/0026-1394/33/2/3.

[37] Y. Zhang, B. Qin, K.C. Chan, R. Lupoi, S. Yin, Y. Xie, S. Ye, P. Yu, H. Ke, W. Wang, Enhancement on mechanical properties of CoCrNi medium entropy alloy via cold spray additive manufacturing associated with sintering, J. Manuf. Process. 94 (2023) 413–423, https://doi.org/10.1016/j.jmapro.2023.03.017.

[38] K.I. Schwendner, R. Banerjee, P.C. Collins, C.A. Brice, H.L. Fraser, Direct laser deposition of alloys from elemental powder blends, Scr. Mater. 45 (2001) 1123–1129, https://doi.org/10.1016/S1359-6462(01)01107-1.

[39] M.Y. Mendoza, P. Samimi, D.A. Brice, B.W. Martin, M.T. Rolchigo, R. Lesar, P.C. Collings, Microstructures and grain refinement of additive-manufactured Ti-xW alloys, Metall. Mater. Trans. 48 (2017) 3594–3605, https://doi.org/10.1007/s11661-017-4117-7.

[40] S. Wei, P. Wang, L. Zhang, U. Ramamurty, Grain morphologies in additively manufactured alloys: From solidification fundamentals to advanced microstructure control, J. Mater. Sci. Technol. 235 (2025) 133–145, https://doi.org/10.1016/j.jmst.2025.02.033.

[41] M.A. Buhairi, F.M. Foudzi, F.I. Jamhari, A.B. Sulong, N.A.M. Radzuan, N. Muhamad, I.F. Mohamed, A.H. Azman, W.S.W. Harun, M.S.H. Al-Furjan, Review on volumetric energy density: influence on morphology and mechanical properties of Ti6Al4V manufactured via laser powder bed fusion, Prog. Addit. Manuf. 8 (2023) 265–283, https://doi.org/10.1007/s40964-022-00328-0.

[42] J. Li, D. Ouyang, Q. Wang, Q. Teng, C. Cai, Q. Wei, Achieving superior tensile strength of $CoCrFeNiTi_{0.3}$ high-entropy alloy via in-situ laser powder bed fusion of CoCrFeNi and Ti, Mater. Sci. Eng. A 886 (2023) 145649, https://doi.org/10.1016/j.msea.2023.145649.

[43] H. Tang, P. Niu, J. Kang, R. Li, T. Yuan, Hierarchically microstructure endowing high strength-ductility synergy in CoCrNi medium entropy alloy fabricated by laser powder bed fusion, Mater. Sci. Eng. A 940 (2025) 148506, https://doi.org/10.1016/j.msea.2025.148506.

[44] D. Wang, C. Song, Y. Tang, Y. Bai, Investigation of crystal growth mechanism during selective laser melting and mechanical property characterization of 316L stainless steel parts, Mater. Des. 100 (2016) 291–299, https://doi.org/10.1016/j.matdes.2016.03.111.

[45] X.W. Liu, J.Q. Yao, X.N. Ma, Y.S. Wang, N. Gao, Y. Shi, Z.T. Fan, H. Du, Columnar-to-equiaxed transition and grain refinement by solute interaction effects, Mater. Charact. 205 (2023) 113288, https://doi.org/10.1016/j.matchar.2023.113288.

[46] W. Zhao, Y. Sun, P. Che, Z. Ning, H. Fan, H. Yang, J. Sun, P.K. Liaw, A.H.W. Ngan, Y. Huang, The columnar to equiaxed transition of CoCrNi medium-entropy alloy fabricated by laser directed energy deposition, Mater. Des. 237 (2024) 112538, https://doi.org/10.1016/j.matdes.2023.112538.

[47] J.D. Hunt, Steady state columnar and equiaxed growth of dendrites and eutectic, Mater. Sci. Eng. 65 (1984) 75–83, https://doi.org/10.1016/0025-5416(84)90201-5.

[48] S.B.A. Malladi, D. Riabov, S. Guo, L. Nyborg, Additive manufacturing of interstitial nitrogen-strengthened CoCrNi medium entropy alloy, Adv. Eng. Mater. 26 (2024) 2401182, https://doi.org/10.1002/adem.202401182.

[49] S.Y. Ahn, S.G. Jeong, M.J. SaGong, G. Lee, E.S. Kim, H. Park, J.-W. Cho, J.G. Kim, H.S. Kim, Size matters: Exploring part size effects on microstructure, defects, and mechanical property in optimized laser powder bed fusion (L-PBF) additive manufacturing, Mater. Sci. Eng. A 902 (2024) 146616, https://doi.org/10.1016/j.msea.2024.146616.

[50] S. Xu, T. Kusama, X. Xu, H. Huang, T. Omori, J. Xie, R. Kaisuma, Large [001] single crystals via abnormal grain growth from columnar polycrystal, Materialia 6 (2019) 100336, https://doi.org/10.1016/j.mtla.2019.100336.

[51] W. Kurz, C. Bezençon, M. Gäumann, Columnar to equiaxed transition in solidification processing, Sci. Technol. Adv. Mater. 2 (2001) 185–191, https://doi.org/10.1016/S1468-6996(01)00047-X.

[52] A. Durga, N.H. Pettersson, S.B.A. Malladi, Z. Chen, S. Guo, L. Nyborg, G. Lindwall, Grain refinement in additively manufactured ferritic stainless steel by in situ inoculation using pre-alloyed powder, Scr. Mater. 194 (2021) 113690, https://doi.org/10.1016/j.scriptamat.2020.113690.

[53] M. Gäumann, C. Bezençon, P. Canalis, W. Kurz, Single-crystal laser deposition of superalloys: processing-microstructure maps, Acta Mater. 49 (2001) 1051–1062, https://doi.org/10.1016/S1359-6454(00)00367-0.

[54] J. Shinjo, A. Kutsukake, A. Arote, Y.T. Tang, D.G. McCartney, R.C. Reed, C. Panwisawas, Physics-based thermal-chemical-fluid-microstructure modelling of in-situ alloying using additive manufacturing: Composition-microstructure control, Addit. Manuf. 64 (2023) 103428, https://doi.org/10.1016/j.addma.2023.103428.

[55] H. Zhang, Y. Lu, X. Wu, J. Zhang, D. Hao, Y. Tao, L. Hu, D. Qi, K.N. Campo, S. Guo, Achieving complete columnar-to-equiaxed transition in laser-processed AlCoCrFeNi alloys via mixed powder preparation, Scr. Mater. 277 (2026) 117223, https://doi.org/10.1016/j.scriptamat.2026.117223.

[56] Y. Lu, H. Zhang, D. Hao, Y. Tao, Z. Dong, K.N. Campo, S. Guo, Simultaneous enhancement of hardness and fracture resistance in aged AlCoCrFeNi high-entropy alloy coatings via mixed-powder laser cladding, Intermetallics 194 (2026) 109299, https://doi.org/10.1016/j.intermet.2026.109299.

[57] H.-J. Lu, W.-B. Wang, N. Zou, J.-Y. Shen, X.-G. Lu, Y.-L. He, Thermodynamic modeling of Cr-Nb and Zr-Cr with extension to the ternary Zr-Nb-Cr system, Calphad 50 (2015) 134–143, https://doi.org/10.1016/j.calphad.2015.06.002.

[58] M. Bernhard, P. Presoly, C. Bernhard, S. Hahn, S. Ilie, An assessment of analytical liquidus equations for Fe-C-Si-Mn-Al-P-alloyed steels using DSC/DTA techniques, Metall. Mater. Trans. B 52 (2021) 2821–2830, https://doi.org/10.1007/s11663-021-02251-1.

[59] W.J. Boettinger, U.R. Kattner, K.W. Moon, J.H. Perepzko, DTA and heat-flux DSC measurements of alloy melting and freezing, in: J.-C. Zhao (Ed.), Methods for Phase Diagram Determination, Elsevier Science Ltd, 2007, pp. 151–221, https://doi.org/10.1016/B978-008044629-5/50005-7.

[60] E.B. Ferreira, M.L. Lima, E.D. Zanotto, DSC method for determining the liquidus temperature of glass-forming systems, J. Am. Ceram. Soc. 93 (2010) 3757–3763, https://doi.org/10.1111/j.1551-2916.2020.03976.x.

[61] G.L. Brollo, C.T.W. Proni, L.C. de Paula, E.J. Zoqui, An alternative method to identify critical temperatures for semisolid materials process applications using differentiation, Thermochim. Acta 651 (2017) 22–33, https://doi.org/10.1111/j.1551-2916.2020.03976.x.

[62] W. Banda, G.A. Georgalli, C. Lang, J.J. Eksteen, Liquidus temperature determination of the Fe-Co-Cu system in the Fe-rich corner by thermal analysis, J. Alloy. Compd. 461 (2008) 178–182, https://doi.org/10.1016/j.jallcom.2007.07.045.

[63] Z. Han, J. Liu, Y. He, K. Li, Y. Ji, J. Liu, Determination of the liquidus and solidus temperatures of FeCrAl stainless steel, Int. J. Miner. Metall. Mater. 22 (2015) 1141–1148, https://doi.org/10.1007/s.12613-015-1178-8.

[64] L. Benazzouz, A. Loucif, G. Brionne, C. Zhang, P.I. Gallego, J.-B. Lévesque, N. Boutarek-Zaourar, M. Jahazi, Assessing the influence of DSC parameters on accurate determination of liquidus and solidus temperatures of a medium carbon low-alloy steel, J. Phase Equilib. Diffus. 46 (2025) 119–132, https://doi.org/10.1007/s11669-025-01178-3.

[65] N. Gao, X.W. Liu, Z.H. Yin, Y.S. Wang, J.Q. Yao, Z.T. Fan, Y. Yang, Design solutes to achieve columnar-to-equiaxed transition and grain refinement in cast multi-principal-element alloys, Metall. Mater. Trans. A 55 (2024) 1397–1408, https://doi.org/10.1007/s11661-024-07316-9.

[66] D.M. Herlach, S. Binder, P. Galenko, J. Gegner, T. Volkmann, Containerless undercooled melts: Ordering, nucleation, and dendrite growth, Metall. Mater. Trans. A 46 (2015) 4921–4936, https://doi.org/10.1007/s11661-015-3052-8.

[67] L.S.E. Teggin, R.F. Chchrane, S.L. Micklethwaite, Z.P. Aslam, A.E. Nassar, A. M. Mullis, Solid-state decomposition following partitionless solidification in dendrite arms of rapidly solidified $CoCrCuFeNi_{0.8}$ high-entropy alloy, Acta Mater. 289 (2025) 120858, https://doi.org/10.1016/j.actamat.2025.120858.

[68] N. Ren, J. Li, R. Zhang, C. Panwisawas, M. Xia, H. Dong, J. Li, Solute trapping and non-equilibrium microstructure during rapid solidification of additive manufacturing, Nat. Commun. 14 (2023) 7990, https://doi.org/10.1038/s41467-023-43563-x.

[69] Z. Fan, F. Gao, L. Zhou, S.Z. Lu, A new concept for growth restriction during solidification, Acta Mater. 152 (2018) 248–257, https://doi.org/10.1016/j.actamat.2018.04.045.

[70] X. Shi, S.-C. Duan, W.-S. Yang, H.-J. Guo, J. Guo, Effect of cooling rate on microsegregation during solidification of superalloy Inconel 718 under slow-cooled conditions, Metall. Mater. Trans. B 49 (2018) 1883–1897, https://doi.org/10.1007/s11663-018-1169-z.

[71] M.J. Aziz, Model for solute redistribution during rapid solidification, J. Appl. Phys. 53 (1982) 1158–1168, https://doi.org/10.1063/1.329867.

[72] M.J. Aziz, W.J. Boettinger, On the transition from short-range diffusion-limited to collision-limited growth in alloy solidification, Acta Matell. Mater. 42 (1994) 527–537, https://doi.org/10.1016/0956-7151(94)90507-X.

[73] R. Brooke, D. Zhang, D. Qiu, M.A. Gibson, M. Easton, Compositional criteria to predict columnar to equiaxed transitions in metal additive manufacturing, Nat. Commun. 16 (2025) 5710, https://doi.org/10.1038/s41467-025-60162-0.

[74] L. Han, Z. Sun, W. Xia, S.-P. Tsai, X. Zhang, J. Rao, P. Wang, A.C.Y. Ngo, Z. Li, Y. Liu, D. Raabe, Thermodynamics-guided high-throughput discovery of eutectic high-entropy alloys for rapid solidification, Adv. Sci. 11 (2024) 2401559, https://doi.org/10.1002/advs.202401559.

[75] M. Walbrühl, A. Blomqvist, P.A. Korzhvyi, Atomic diffusion in liquid nickel: First-principles modelling, J. Chem. Phys. 148 (2018) 244503, https://doi.org/10.1063/1.502634.

[76] W. Zhai, W. Zhou, S.M.L. Nai, Grain refinement of 316L stainless steel through in-situ alloying with Ti in additive manufacturing, Mater. Sci. Eng. A 840 (2022) 142912, https://doi.org/10.1016/j.msea.2022.142912.

[77] Y. Liu, L. Xu, C. Qiu, Development of an additively manufactured metastable beta titanium alloy with a fully equiaxed grain structure and ultrahigh yield strength, Addit. Manuf. 60 (2022) 103208, https://doi.org/10.1016/j.addma.2022.103208.

[78] Y. Ren, Z. Li, Q. Wang, J. Liu, L. Zhang, M. Song, S. Liu, S. Guo, Z. Jiao, I. Baker, H. Wu, Effect of Nb content on microstructural evolution, mechanical and tribological properties of in situ alloyed copper-modified titanium produced using laser powder bed fusion, J. Mater. Sci. Technol. 219 (2025) 257–270, https://doi.org/10.1016/j.jmst.2024.07.038.

[79] L. Chechik, I. Todd, Inconel 718 two ways: powder bed fusion vs. directed energy deposition, Addit. Manuf. Lett. 6 (2023) 100145, https://doi.org/10.1016/j.addlet.2023.100145.

[80] M.V. Pantawane, Y.-H. Ho, S.S. Joshi, N.B. Dahotre, Computational assessment of thermokinetics and associated microstructural evolution in laser powder bed fusion manufacturing of Ti6Al4V alloy, Sci. Rep. 10 (2020) 7579, https://doi.org/10.1038/s41598-020-63281-4.

[81] D.Y. Sun, M. Asta, J.J. Hoyt, M.I. Mendelev, D.J. Srolovitz, Crystal-melt interfacial free energies in metals: fcc versus bcc, Phys. Rev. B 69 (2004) 020102, https://doi.org/10.1103/PhysRevB.69.020102.

[82] J.J. Hoyt, M. Asta, T. Haxhimali, A. Karma, R.E. Napolitano, R. Trivedi, B.B. Laird, J.R. Morris, Crystal-melt interfaces and solidification morphologies in metals and alloys, MRS Bull. 29 (2004) 935–939, https://doi.org/10.1557/mrs2004.263.